Acta Materialia 282 (2025) 120516

Contents lists available at ScienceDirect

Acta Materialia

journal homepage: www.elsevier.com/locate/actamat

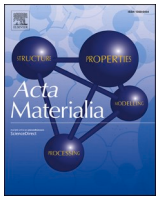

Unusual deformation mechanisms evoked by hetero-zone interaction in a heterostructured FCC high-entropy alloy

Jiahao Li [a], Xinkai Ma [a,*], Kejie Lu [a], Yanfei Wang [b,*], Yuntian Zhu [c,*]

[a] Key Laboratory of Advanced Technologies of Materials, Ministry of Education, School of Materials Science and Engineering, Southwest Jiaotong University, Chengdu, Sichuan 610031, China
[b] State Key Laboratory for Strength and Vibration of Mechanical Structures, School of Aerospace Engineering, Xi'an Jiaotong University, Xi'an 710049, China
[c] Department of Materials Science & Engineering, City University of Hong Kong, Kowloon 999077, Hong Kong, China

ARTICLE INFO

Keywords:
Heterostructure
Strength-ductility combination
Hetero-deformation induced stress
Hetero-zone boundaries affected region
High entropy alloy

ABSTRACT

Understanding the synergistic mechanical effects of heterostructured materials remains challenging due to the complexities in the underlying deformation mechanisms, which are usually diverse, activated at different length scales and possibly interacting. Here, we unravel a deformation fundamental for heterostructures: in addition to the direct contribution on strength, hetero-zone interaction and the development of long-range internal stress could assist in evoking extra plastic mechanisms that are difficult to activate in their homogeneous counterparts. Specifically, the deformation of a heterostructure in $Al_{0.1}CoCrFeNi$ alloy, featuring nanostructured hard lamellae embedded in fine-grained soft matrix, is taken as an example for study. Drawing from experimental insights, the long-range internal stress buildup at elastoplastic transition stage due to intense dislocation pile-ups against hetero-zone boundary, which increases yield strength significantly, is theoretically analyzed. At the plastic stage, the high internal stress helps to activate phase transformation in the fine-grained zones, and the inter-zone constraint leads to form dispersed stable strain bands in the nanostructured zones. These extra mechanisms, together with enhanced deformation twinning, facilitate work hardening and coordinate the strain partitioning between zones, imparting improved ductility at high flow stress. These findings indicate a principle for heterostructural design: introducing strong hetero-zone interaction to enhance internal stress and thereby invoke new deformation mechanisms.

1. Introduction

Structural metallic materials used in safety-critical engineering are expected to be strong and ductile, as high strength contributes to energy efficiency and good ductility prevents catastrophic failure [1]. However, these two properties are rarely attainable at the same time [2]. For instance, high strength even over 1 GPa can be readily attained by refining grain size to nanoscale, but this is inevitably accompanied by the sacrifice of ductility [3]. The crux behind this tradeoff dilemma lies in the exhaustion of strain hardening capability when increasing strength. Plastic instability and damage localization initiate when the strain hardening rate can no longer keep up with flow stress [4]. In this regard, there are logically several potential routes towards strength-ductility synergy: (*i*) activate strong work hardening mechanism into high-strength material without conceding too much strength, (*ii*) introduce extra strengthening mechanism for the one with moderate strength and sufficient work hardening room, and (*iii*) combine the first two routes. The realization of these routes poses a great challenge in innovating microstructure design.

Inspired by the heterostructure in tough biological systems, researchers have recently tried to build heterogeneous microstructure in metals [5-7]. Improved strength and ductility, even superior to what is predicted by rule-of-mixtures, were indeed achieved in a variety of heterostructured metals [8-10]. For instance, heterostructured Cu and Ti, with micrometer-sized grains dispersed in nanostructure (NS) matrix, were found to possess comparable strength to freestanding NS while being as ductile as their coarse-grained (CG) counterparts [10,11]. Such extraordinary properties indicate a unique opportunity conferred by heterostructure design for overcoming the above challenge, which actually implements route (*iii*). Meanwhile, a fundamental distinguishes between successful heterostructure design and conventional composites is that, in addition to the inherent advantages of combining the

* Corresponding authors.
E-mail addresses: sdutmakai@swjtu.edu.cn (X. Ma), yfwang@xjtu.edu.cn (Y. Wang), y.zhu@cityu.edu.hk (Y. Zhu).

https://doi.org/10.1016/j.actamat.2024.120516
Received 8 September 2024; Received in revised form 23 October 2024; Accepted 25 October 2024
Available online 26 October 2024

constituent regions, there should be extra strengthening and work hardening caused by the synergistic interaction between heterogeneous zones, which has been referred to as synergistic mechanical effects [6,11,12].

Obviously, understanding the physical origins of the synergistic mechanical effects is essential to elucidating the design principle of advanced heterostructures. However, it remains challenging as well due to the complexities of synergistic deformation mechanisms. The deformation incompatibility causes inter-zone interaction, which directly changes the zone-scale stress/strain status, especially in the regions near zone boundary, and thus affects local crystallographic mechanisms [13-15]. Specifically, the complexity of synergistic deformation mechanisms usually is manifested in the following aspects. First, they are usually diverse, depending on the material and deformation stage as these factors dictate the manner and intensity of inter-zone interaction [16,17]. For instance, multiple unusual mechanisms were found to be activated sequentially by hetero-zone interaction in a heterostructured CrCoNi [18]. Second, they may be activated at different length scale, such as that across zones or limited near zone boundary, since the short-/long-range internal stresses are affected simultaneously [19,20]. Third, the unusual deformation mechanisms may provide feedback to the development of internal stress, which makes it possible for them to influence each other even if they are active at different deformation stages. For example, the pileup of geometrically necessary dislocations (GNDs) and concomitant development of back stress at elastoplastic transition may promote the accumulation of forest dislocations [11,19,21], facilitate mechanical twinning [17,22], or even affect the nucleation of micro damages [6,23].

Despite the complexity, some significant advances have been made in understanding the synergistic deformation mechanisms. From the perspective of material physics, a widely recognized mechanism was proposed by Zhu and Wu et al. [6,24]. They suggested that the pileup of GNDs near zone boundary and the resulting long-range internal stress are primarily responsible for the extra strengthening and work hardening. Within this framework, the hetero-zone boundary affected region, i.e., the GND building-up region, was found to be a primary microstructural factor controlling the extra mechanical responses [11,25]. This mechanism addressed the roles of long-range internal stress and zone boundary. However, it ignores the effects of possible interaction between long-range internal stress and other possible mechanisms, and there is no consideration on zone-scale strain accommodation. Coincidentally, some synergistic mechanisms exclusive to specific heterostructured materials were also observed, such as the formation of dislocation bundles in gradient nanotwined Cu and sequentially twinning in heterostructured $Fe_{20}Co_{20}Ni_{41}Al_{19}$ alloy [8,17]. From the perspective of mechanics, the most significant synergistic behaviors at zone scale involves load/strain partitioning among zones [26,27], dynamic inter-zone constraint [16] and strain gradient development near hetero-zone boundary [13], which create inhomogeneous internal stress such as superimposing back stress and change the paths of strain/-damage evolution [28,29]. Although many constitutive modeling has been conducted for the trans-scale mechanics [30,31], physics-based model providing simultaneous insights into the synergistic deformation mechanisms and their coupling is still largely lacking.

Despite previous efforts, the deformation fundamentals and the physics behind the extraordinary mechanical effects are not fully understood. The crux lies in the complexity of synergistic deformation mechanisms. Several further issues have emerged from recent advances: how does long-range internal stress interact with other potential or prevalent mechanisms? How does hetero-zone interaction affect strain accommodation? The second issue involves the coordination and partitioning of applied strain at micro scale, which is closely related to the nucleation and evolution of strain localization.

It may be difficult to thoroughly address these issues in a single work, since the deformation mechanisms depend on the type of heterostructure and the material. Therefore, one of the most common heterostructures in an initially single-phase face-centered cubic (fcc) alloy was taken as an example to probe the key fundamental behind the issues. Specifically, partially recrystallized $Al_{0.1}$CoCrFeNi alloy was synthesized to work with, by combining experimental observations in the synergistic mechanical responses and plastic mechanisms, theoretical analyses in the development of internal stress and the activation condition of potential mechanisms. The results proved that hetero-zone interaction and long-range internal stress could also assist in evoking potential plastic mechanisms that are inaccessible to homogeneous structures.

2. Experiments

2.1. Preparation of heterostructure and the homogeneous counterparts

$Al_{0.1}$CoCrFeNi high-entropy alloy was taken as an example to build heterostructure for the following reasons. First, it exhibits excellent mechanical properties over 77–298 K and the good metallurgical formability [32-35]. Second, the deformation mechanism of homogeneous counterparts is relatively simple and well known, usually involving only dislocations, twinning and stacking faults (SFs), even at cryogenic temperature [34,36,37]. Third, it has relatively low stacking fault energy, estimated to be ~18 mJ/m^2 at 298 K and ~12 mJ/m^2 at 77 K by averaging literature records and considering the temperature dependence as suggested by Saeed-Akbari et al. [38-41], which confers the potential of evoking additional mechanisms, such as phase transformation if encountered with exceptionally high stresses.

The raw material was prepared by suspension melting of elemental ingredients (purity >99.9 wt.%) in high-purity argon atmosphere. To ensure uniformity, the ingot was re-melted at least five times. Then, the as-cast ingot was homogenized at 1200 °C for 24 h followed by air cooling. Finally, a measured composition of 2.11Al-25.59Co-23.63Cr-25.43Fe-23.24Ni (at.%) was determined by energy disperse spectroscopy. The heterostructure was produced by cold rolling and partial recrystallization. The as-homogenized material was rolled to 0.5 mm thick after 20 rolling passes with a thickness reduction of 90 %, using a customized machine with rolls fully immersed in liquid nitrogen, to obtain severely refined nanostructure with as high as possible stored energy. By trial and error, the annealing parameters for expected heterostructure, 550 °C for 1 hour followed by air cooling, were identified, by which the resulting microstructure of constituent zones conforms to the key design principles of strong-yet-tough material. To examine the mechanical effects caused by heterostructure, its performances are compared with those of the homogeneous structures with identical microstructure as the constituent zones in heterostructure. A set of homogeneous materials were thus screened from a wide range of annealing conditions.

2.2. Mechanical tests

Dog-bone-shaped tensile samples with gauge dimensions of $10 \times 3 \times 0.5$ mm^3 (length × width × thickness) were machined from as-processed sheets, with the length aligned with the rolling direction. Uniaxial tension at a nominal strain rate of 1×10^{-3} s^{-1} were performed at 77 K, in order to amplify the synergistic mechanical effects by promoting GNDs piling-up. In the tests at 77 K, samples were immersed in liquid nitrogen throughout the whole process. Three samples were tested for each type of material to guarantee the reliability of results. Hardness measurements for each sample were conducted with >60 indentations under a load of 50 g and a dwell time of 10 s. The sample for hardness test was electropolished and then subjected to metallographic corrosion so as to identify which type of constituent zone the indentation was located using an optical microscopy. The spacing of neighboring indentations was three times longer than impression diagonal.

2.3. Microstructure and microscale strain characterizations

Microstructures before and after tensile tests were examined using field emission scanning electron microscope (FE-SEM, Quanta FEG 250) equipped with Oxford-electron backscatter diffraction (EBSD) system and transmission electron microscopies (TEM, both FEI Titan Cube 80–300 and JEOL JEM-2100F), to analyze the microstructure heterogeneity-dictated deformation mechanisms. EBSD data was analyzed using the Oxford-HKL Channel 5 and OIM software, where grain detection tool can be used to evaluate the grain size and corresponding area fractions. Twin boundaries in recrystallized grains were not counted as grain boundaries in grain size determination. TEM, high resolution-TEM (HR-TEM), and scanning TEM (STEM) observations were conducted at an accelerating voltage of 200 kV. TEM foils were first mechanically ground to a thickness of ~70 μm, followed by electropolishing with 90 % ethanol and 10 % perchloric acid at 25 V and −25 °C. Samples for EBSD examinations were electropolished in an electrolyte composed of 90 % ethanol and 10 % perchloric acid for 60–75 s at 20 V.

In the tension of heterostructure at 77 K, the test was interrupted as pre-specified strain stages and the sample was then carefully transferred into SEM to map the distribution of microscale strain in the same region of interest, using μ-DIC technique. Before the initial loading, the region of interest was marked using carbon deposition and the grain morphology was recorded using EBSD. High-quality speckles were then prepared through silver plating and NaCl solution immersion. The reference speckle pattern of the region of interest was captured in secondary electron mode. Subsequently, speckle image at different strain stages were captured under the same parameters.

3. Results

3.1. Heterogeneous microstructure

Fig. 1 shows the microstructural details of as-processed heterostructure. It has the typical characteristic of partial recrystallization: non-recrystallized lamella embedded in recrystallized matrix (Fig. 1a) with well-defined hetero-zone boundaries (HBs, Figs. 1b& c). Microstructural heterogeneities exist in the following aspects. (*i*) Recrystallized matrix is characterized by equiaxed fine grains (FG) with an average size of ~2.4 μm (Figs. 1d& e), while NS remains in non-recrystallized lamella (Fig. 1c). (*ii*) The clean interior of recrystallized FGs is in sharp contrast to the latter which has extremely high dislocation density (Figs. 1b& c). (*iii*) Recrystallized FGs have relatively random orientation, while non-recrystallized lamella is highly textured, with <101>//rolling direction (Figs. 1a& F). Statistics from a series of back-scattered electron images confirms a volume fraction of ~38 % for the non-recrystallized lamella.

Interestingly, these microstructure features are consistent with the key design principles of strong-yet-tough heterostructure. First, dramatic heterogeneities produce high mechanical incompatibility between zones, as verified by the large hardness difference (the red data in Fig. 2a), which helps to improve the intensity of hetero-zone interaction [14,42]. Second, the lamella morphology of non-recrystallized zone confers higher density of HBs, which is highly expected to promote GND piling-up and consequently the effect of hetero-zone boundary affected region [11,15]. Third, the grain size of recrystallized zone is close to the critical dimension delineated by strain energy density maximization principle, i.e., the optimum grain size for strength-ductility combination ($d_{optimal} \sim 2\ \mu m$, Fig. 2b), which ensures excellent intrinsic properties for constituent zone and thus helps to improve global performances [43, 44]. Note that strain energy density maximization principle is a general mechanics principle that can guide microstructure regulation, such as grain size design, to unify the highest possible strain energy density limit and strength [44].

Three types of homogeneous materials were prepared. As shown in Figs. 3a1-a2, a homogeneous NS experienced recovery but almost no recrystallization, which closely resembles the non-recrystallized zone in heterostructure (Fig. 1c), was synthesized by annealing as-rolled sheets at 475 °C for 1 h Hardness examination confirms that it does have comparable hardness to the non-recrystallized zone in heterostructure (Fig. 2f). A fully recrystallized FG structure, whose grain morphology (Figs. 3b1-b2), average grain size (2.1 μm, Fig. 3d) and hardness (Fig. 2b) are consistent with those of the recrystallized matrix in the heterostructure, was produced by annealing at 600 °C for 1 h Since both the microstructure and hardness are in good agreement, the deformation responses of such homogeneous NS and FG samples can, respectively, represent the intrinsic properties of the non-recrystallized hard zone and recrystallized soft matrix, i.e., the properties of constituent zones when they are deformed independently. Moreover, a CG structure in average grain size of 8.5 μm was prepared as well (Figs. 3c& e).

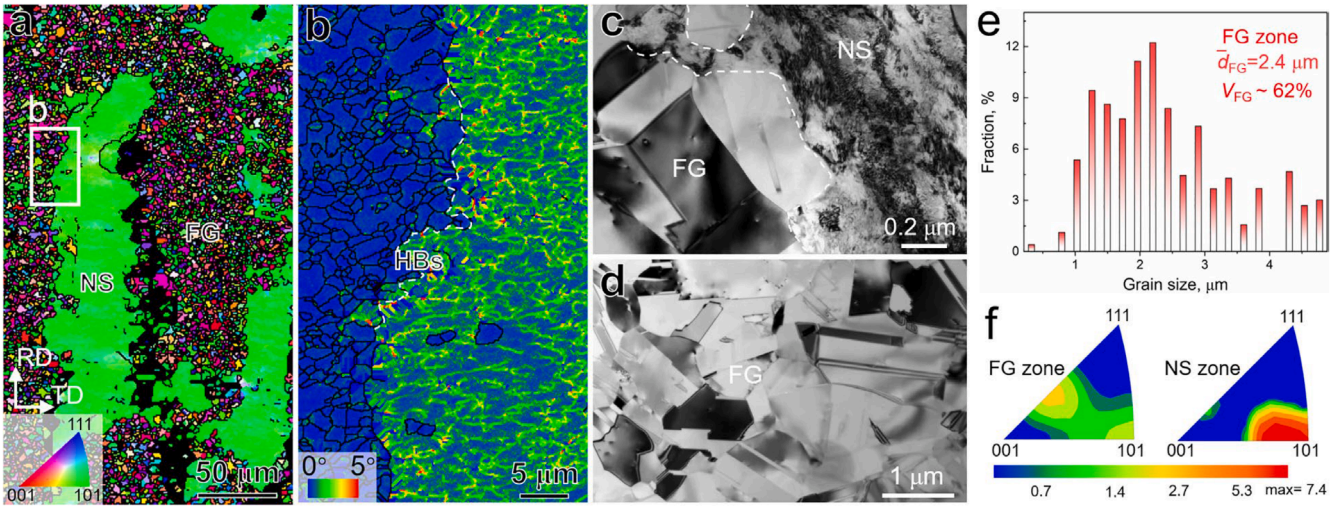

Fig. 1. Heterostructure in $Al_{0.1}CoCrFeNi$ alloy, produced via cryogenic rolling followed by annealing at 550 °C for 1 h (a) EBSD inverse pole figure showing non-recrystallized lamella (the hard zone) embedded in recrystallized matrix (the soft zone). (b) Local kernel average misorientation map and (c) representative TEM image showing well-defined HBs and high contrast in dislocation density across them. (d) TEM image showing equiaxed FGs in recrystallized zone. (e) Grain size distribution of the FG zone. (f) Pole figures showing the texture heterogeneity between FG and NS zones.

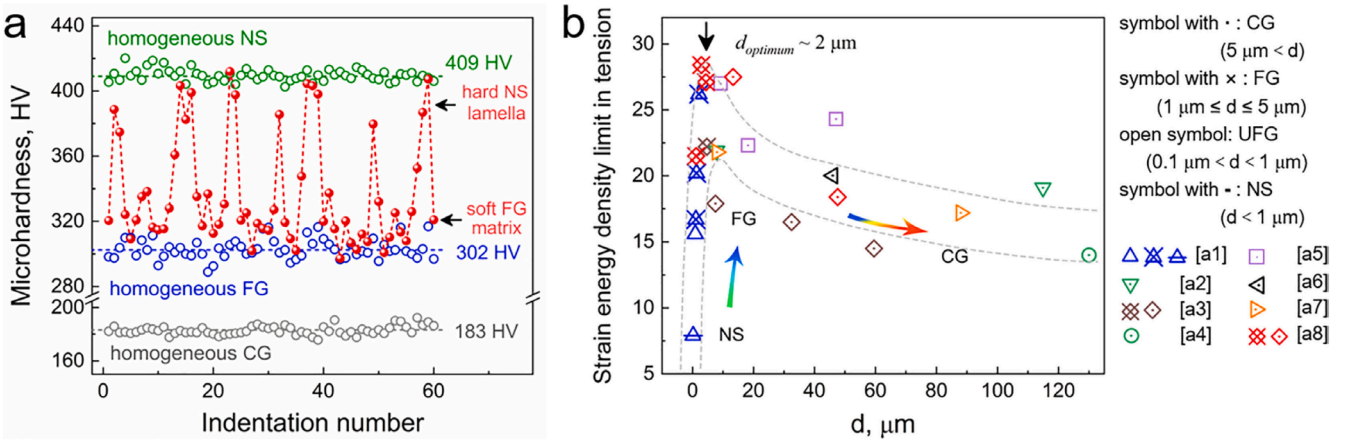

Fig. 2. (a) Microhardness distribution in heterostructure (red) and the homogeneous counterparts, showing that the hardness of FG matrix and NS lamella are comparable to that of homogeneous FG and NS samples, respectively. In the test of heterostructure, the location of every impression in FG matrix or NS lamella was carefully confirmed, and if the one crosses HB it is deleted. (b) Strain energy density limit ($\sim \delta_u * (\sigma_y + \sigma_{uts})/2$), versus grain size d in $Al_{0.1}CoCrFeNi$ with homogeneous microstructure, showing the $d_{optimum} \sim 2\ \mu m$ for strength-ductility synergy [43,44]. δ_u, σ_y and σ_{uts} are the uniform elongation, yield strength and ultimate strength, respectively. Literature a1-a8 are [45,34,46,37,47,35,48] and [49], respectively. (For interpretation of the references to colour in this figure legend, the reader is referred to the web version of this article.)

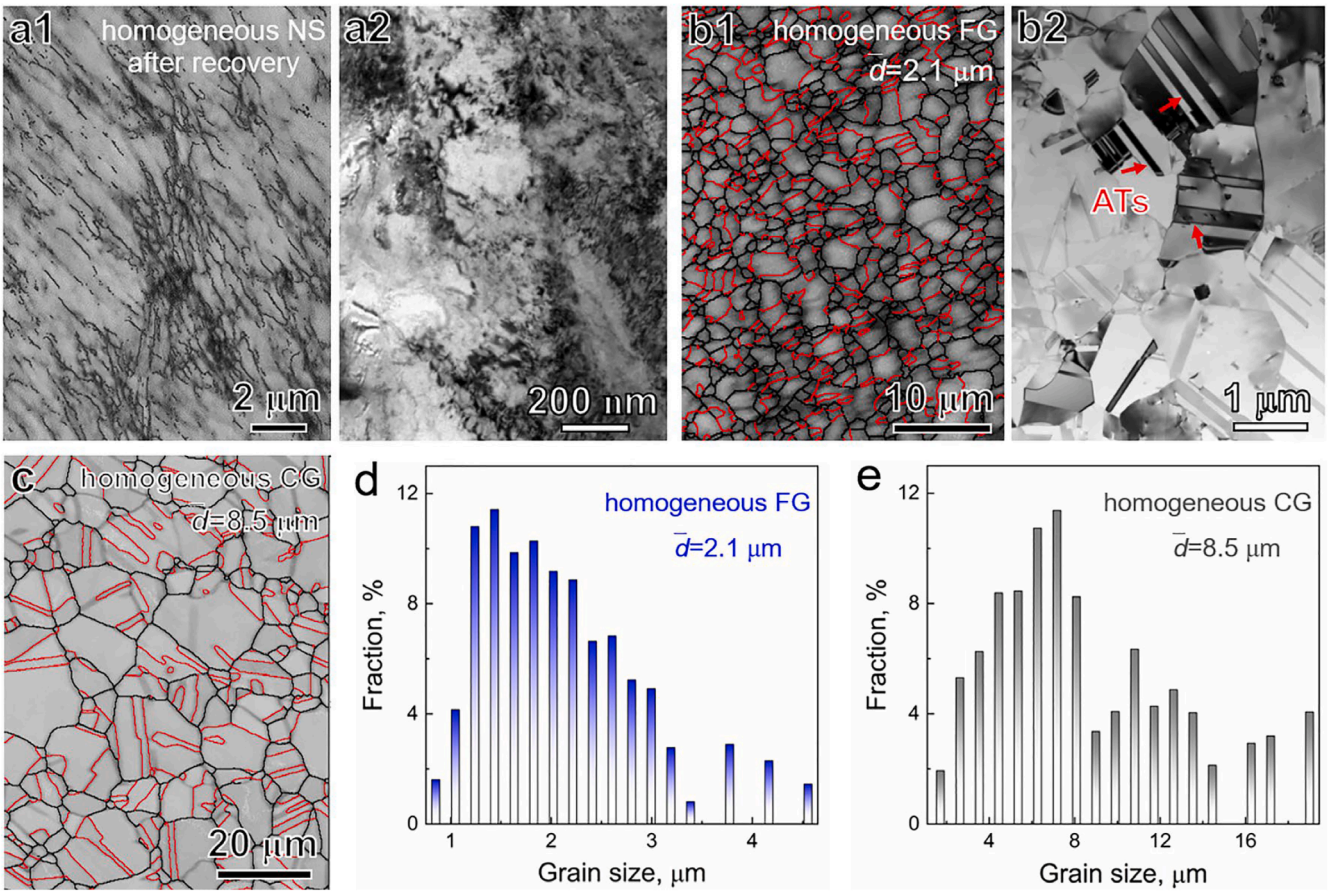

Fig. 3. Homogeneous microstructure of control samples. (a1, a2) EBSD band contrast map and representative TEM image showing recovered homogeneous NS obtained by annealing at 475 °C for 1 h (b1, b2) Band contrast map and TEM image showing fully recrystallized FG sample (by annealing at 600 °C for 1 h). (c) Homogeneous CG sample (1000 °C for 5 min). Statistical distribution of grain size for (d) homogeneous FG and (e) homogeneous CG samples.

3.2. Synergistic mechanical effects dictated by microstructure heterogeneity

For the purpose of enhancing the synergistic deformation mechanisms and their interaction, uniaxial tensions were performed at 77 K (Fig. 4a1), since reduced temperature usually suppresses cross slip and thus promotes planar piling-up of GNDs, which consequently improves long-range internal stress [22,50]. For comparison, tests at 298 K were performed (Fig. 4a2). The yield strength of heterostructure at 298 K (1015 ± 5 MPa) is measured to be close to the volume fraction-weighted

average (~1010 MPa) based on the properties of homogeneous NS and FG samples, i.e., the prediction by rule-of-mixtures [10]. Although in contrast to recent experimental advances in synergistic strengthening, this is actually not an anomaly and has also been observed in some multimodal and laminate heterostructures [51,52]. The possible reason is that an easily activated mechanism intrinsic to a constituent zone, such as shear localization in NS zone, dominates the deformation and releases internal stress, which shields or offsets the synergistic mechanical effects from hetero-zone interaction [53]. Since such effect is often material and microstructure dependent, it should also exist in the deformation at 77 K to some extent. Comparing the yield strength increment as temperature decrease ($\sigma_y^{77K} - \sigma_y^{298K}$) between heterostructure and homogeneous samples, therefore, should be a more objective way to analyze synergistic strengthening at 77 K.

Fig. 4b1 presents a plot of $\sigma_y^{77K} - \sigma_y^{298K}$ against grain size, where the equivalent grain size of heterostructure is calculated as the volume fraction-weighted average of the grain size of constituent zones. As shown, heterostructure has an unusually high $\sigma_y^{77K} - \sigma_y^{298K}$, deviating significantly from the evolution law of $\sigma_y^{77K} - \sigma_y^{298K}$ with grain size change in homogeneous materials. Such deviation, indicated by $\sigma_{y,extra}$ in Fig. 4b1, indicates a pronounced enhancement of the extra strengthening induced by microstructure heterogeneity at 77 K. Since the apparent synergistic strengthening at 298 K is negligible, the $\sigma_{y,extra}$ actually can also be considered as a conservative evaluation of synergistic strengthening at 77 K. The $\sigma_{y,extra}$ accounts for ~9 % of global yield strength (1242 ± 10 MPa), making it much higher than the prediction by rule-of-mixtures (~1140 MPa). Note that such enhanced synergistic strengthening at cryogenic temperature is also found in heterostructured CrCoNi and FeMnCrCoNi alloys (Fig. 4b2), implying that it may be a general behavior in heterostructured fcc materials.

The uniform elongation of heterostructure is as high as 32.2 %±3.4 %, increased by ~167 % as compared to the performance at 298 K, which is much higher than the increase of homogeneous NS (~10 %) and FG (~80 %) samples (Figs. 4a1 & a2). This could be partially attributed to the extraordinary work hardening of heterostructure, which far exceeds the prediction by rule-of-mixtures (shaded region in Fig. 4c). Importantly, this suggests again that synergistic deformation mechanisms are largely enhanced at 77 K, which helps to suppress the quick instability that may prevalent in a freestanding NS counterpart or in the deformation of heterostructure at 298 K.

3.3. Synergistic deformation mechanisms dictated by microstructure heterogeneity

Such largely enhanced synergistic strengthening, work hardening and ductility implies extensive activation of synergistic deformation mechanisms, which provides a unique opportunity to probing their interaction. The cross-HBs crystallographic and/or micro-mechanical behaviors at different tensile strains under 77 K are therefore examined.

3.3.1. Deformation of recrystallized FG zone in heterostructure

Figs. 5a1-a2 are TEM images obtained at the stress level of ~1000 MPa, at which most of the recrystallized FG should have yielded while the NS zone remain elastic due to stress partitioning [26,65]. Low-density planar dislocations traces (Fig. 5a1) and early pile-ups (Fig. 5a2) appear in the FGs side of HBs. Fig. 5b shows the typical microstructure soon after global yielding (~1.5 % tensile strain). Strong pile-ups in the length scale of a few micrometers against the HBs are observed, suggesting a quick piling up process of GNDs in the yielding procedure. The interior of FGs away from HBs remains relatively clean at this stage, even when the global applied strain increases to ~3 % (Fig. 6a). As plastic deformation proceeds and applied stress increases, more dislocations aligned in the pile-up, exerting higher stress

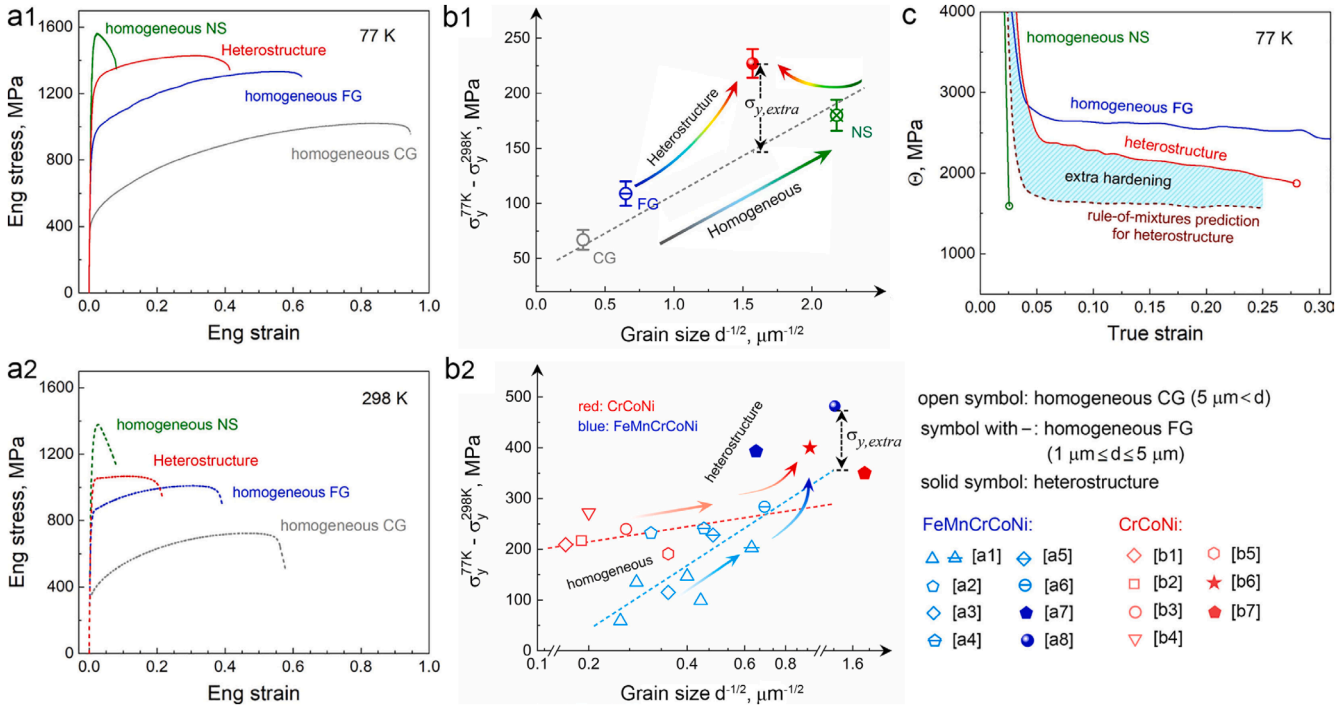

Fig. 4. Synergistic mechanical effects. Engineering (Eng) stress-strain curves of heterostructure and homogeneous samples at (a1) 77 K and (a2) 298 K. (b1) σ_y increment as decreasing temperature ($\sigma_y^{77K} - \sigma_y^{298K}$) plotted as a function of grain size, where the unusually high $\sigma_y^{77K} - \sigma_y^{298K}$ of heterostructure suggests an extra strengthening ($\sigma_{y,extra}$). (b2) Similar extra strengthening in heterostructured CrCoNi and FeMnCrCoNi alloys. (c) Strain hardening rate Θ at 77 K, showing pronounced extra strain hardening displayed by heterostructure. Notes for understanding the above figures are listed. First, the data in (b2) are experimental records (a1-a8: [50, 54-58], b1-b6: [22,59-64]); Second, in (b1) and (b2), the abscissa of the heterostructured sample, namely the equivalent grain size of heterostructure, is estimated as the volume fraction-weighted average of the grain size of constituent zones. Third, the rule-of-mixtures prediction in (c) is calculated as $V_{FG}\Theta_{FG} + V_{NS}\Theta_{NS}$.

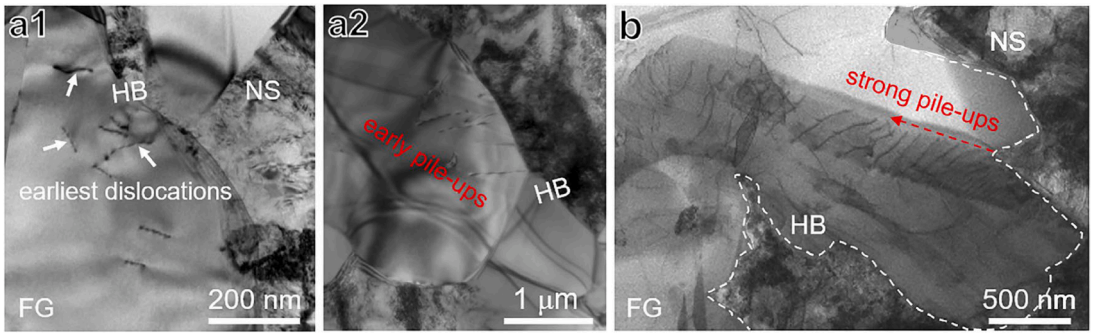

Fig. 5. Representative TEM and STEM images showing the deformation of FG zone in heterostructure near global yielding at 77 K: (a1-a2) interrupted at the stress level of ~1000 MPa, TEM images showing the earliest dislocations traces near HB and early pile-ups against HB, (b) bright-field STEM image of the developed pile-ups in the scale of a few micrometers at a tensile strain of ~1.5 %.

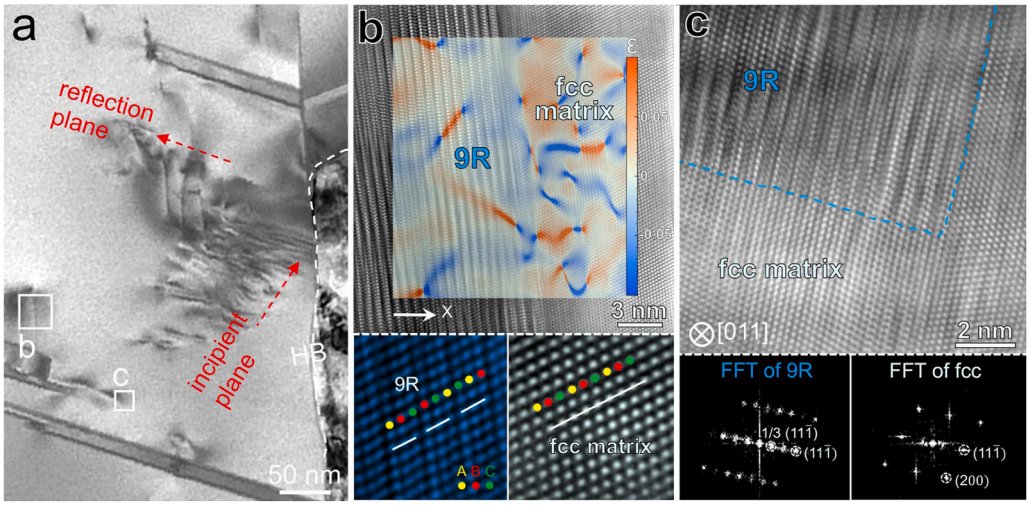

Fig. 6. Deformation behaviors in the FG zone of heterostructure at a tensile strain of ~3 % at 77 K. (a) Dislocations piled up and reflection against HB. (b, c) High-resolution TEM images taken near the head of pile-up along [011] zone axis, showing the formation of 9R phase. The insert in (b) shows the horizontal lattice strain ε_x map. The fast Fourier transformed (FFT) patterns in (c) confirm the coexistence of fcc and 9R phases.

concentration on the HB and the dislocations near pile-up head. The latter will be overwhelmed first and thus cross slip to an intercepting {111} plane if the HB has not yielded [66]. Such behavior is observed at a tensile strain of ~3 % (Fig. 6a).

These HB-dependent deformation behaviors at low-strain stages are in sharp contrast to that in homogeneous structure as presented later, implying some crucial micro-mechanics. First, the HBs are effective obstacle for gliding dislocations. Under a resolved stress of τ_a, the gradient alignment of n dislocations on a slip plane could yield a stress concentration high up to $n\tau_a \sim \pi n\tau_a/4$ at head [67]. The strong pile-up (Fig. 5b) and the cross slip of dislocations near pile-up head (Fig. 6a) indicate a high strength of HBs. Note that although pile-ups can also form against grain or twin boundaries, they generally have no opportunity to withstand such high stress concentration, as the relatively low boundary strength or small cross-boundary strength difference facilitates dislocation absorption and slip transmission [68,69]. In other word, high-strength HB or relatively large strength difference across it is actually a prerequisite for the formation of strong GND pile-ups and consequently the development of high long-range internal stress. Second, the clean interior of FGs indicates that it is largely strengthened by the long-range back stress induced by GND pile-ups [24].

Surprisingly, closer examination of FG zone at ~3 % applied strain unveils the occurrence of new structure near the tail of pile-ups (Figs. 6a-c). Figs. 6b-c show the high-resolution TEM images and the corresponding FFT patterns of such new structure. The pattern indicates a 9R phase in [011] zone axis. This structure can be regarded as a modified fcc structure, characterized by one stacking fault in every three {111} plane [70,71], as evidenced by the high-resolution TEM image (the lower left insert in Fig. 6b). Through the geometric phase analysis of the region of interest (Fig. 6b) [72], it can be seen that the 9R phase accommodates a portion of the applied strain, with a strain fluctuation range approximately 10 %. 9R phase is hardly formed by accidental growth, which is considered to be driven in the high stress region except for the low stacking fault energy [73,74].

As deformation progresses, grain boundaries, phase interfaces and other existing defects act as obstacles for mobile defects, resulting in quick multiplication of defects and continuous increase of internal stress (Fig. 4a1). The increased internal stress is conducive to the activation and slip of Schockley partials that constitute the 9R structure. When the applied strain is increased to ~20 %, 9R phases can be frequently found (Fig. 7a1). Figs. 7a2-a3 show the high-resolution TEM image of 9R/fcc boundary and corresponding IFFT pattern, from which multiple partial dislocations (marked by 'T') can be observed. The partial dislocations act as barriers to block the movement of dislocations at the phase interfaces, thereby enhancing the stability of the 9R phase [75].

Interestingly, at such large-strain stage, transformation to nano-layered hexagonal close-packed (hcp) phase was also evoked in the FG side of HB, as shown in Figs. 7b1-b2 and magnified in Fig. 7b3. Moreover, hcp laths, which adheres to the twinning lamella, are observed in heterostructure as well, as confirmed by the SAED pattern of bright-field

image (Fig. 7c2) and corresponding dark-field image (Fig. 7c3). Such coexistence of twins and hcp is rarely detected in deformation and/or plastic processing of $Al_{0.1}$CoCrFeNi alloy, even in the deformation of optimized heterostructure at room temperature [33], severe plastic deformation generated by surface nanocrystallization [37], and cryogenic deformation of homogeneous FGs (*Section 3.4*). These indicate that, extremely high internal stress, which is unattainable in homogeneous structures, can be generated in the deformation of heterostructure at 77 K to drive fcc→hcp transformation [76,77].

On the other hand, the increased internal stress facilitates the attainment of the critical twinning stress, τ_{TWIP}, which is estimated to be ~320 MPa assuming that it is roughly independent of temperature [78, 79]. As the bright-field TEM images and corresponding diffraction patterns shown in Figs. 8a-b, high-density nanotwins with a spacing of only a few nanometers spread throughout the whole FG zone, which suggests a critical dynamic Hall-Petch effect displayed by deformation twinning at the large-strain stage. Importantly, a statistical comparison unveils that the average nanotwin spacing of FG zone in heterostructure is much smaller than that of homogeneous FG structure (Figs. 8c1 & c2). This confirms that deformation twinning is enhanced as well by the synergistic deformation of heterogeneous microstructure.

3.3.2. Deformation of non-recrystallized NS zone in heterostructure

A long-standing doubt arising from the large hardness/strength difference between NS islands and CG matrix (Fig. 2a) is whether and how the former accommodates applied strain. This may be the key to the second issue discussed above. Fig. 9a presents the cross-HB kernel average misorientation (KAM) maps at ~5 % and ~15 % tensile strain. Statistics reveals that in this strain interval, the average KAM of NS zone increased by ~0.55, which is almost high up to three-quarters of that of FG zone (~0.74, Fig. 9b). This indicates that pronounced plastic strain is partitioned into the hard NS zone, and the quick catastrophic instability that occurred in a freestanding NS counterpart (Fig. 4a1) is effectively avoided here [15,80]. In other words, the synergistic constraint from the soft FG zones makes the NS zones ductile to some extent, and there should be unique plastic mechanisms being activated [81].

Fig. 10 presents the evolution of tensile strain across an HB, providing zone-scale insight into the strain accommodation mechanism of NS zone. Surprisingly, in sharp contrast to the quick coalescence of catastrophic strain localization in a freestanding NS counterpart [3,82, 83], high-density of strain bands (SBs) are dispersively developed over the NS zone, as indicated by white arrows. These SBs undertake most of the strain partitioned into NS zone, with none of them preferentially carrying excessive strain concentration to dominate geometrical softening. In other words, such SBs are plastically stable, i.e., dispersed stable SBs, resulting in delocalized strain accommodation in the NS zone [28,81]. It is also observed that the closer to the HB, the weaker the SBs. These observations confirm several curiosities: (*i*) the mechanism by which the NS zone accommodate large applied strain is forming dispersed stable SBs, (*ii*) SBs mainly nucleate from the interior of NS zone, (*iii*) HBs play a role in impeding SBs propagation, and (*iv*) the activation of this mechanism depends largely on the microstructure heterogeneity and hetero-zone interaction, since there is no such opportunity for its freestanding NS counterpart [82,83].

As strain partitioning progresses, SBs partially propagate into the FG zone with obvious intensity attenuation. This helps to coordinate the deformation incompatibility and alleviate possible mechanical singularity near HB [84]. The initial microstructure of NS zone is mainly characterized by dislocation cells with an average size of ~210 nm with small orientation difference between them, as indicated by the TEM images and SAED pattern (Figs. 11a& b) as well as the misorientation map (Fig. 1a). The most significant microstructure change after tension is the formation of SFs and deformation nanotwins (Figs. 11c& d). Nevertheless, similar to the deformation of NS bronze layer in a laminate [81], the density of SFs and deformation twins is not yet very high. This implies that the deformation of strain banding region may be partially dependent on dislocation and grain boundary activities [28].

3.4. Deformation mechanism of homogeneous FG and NS

In homogeneous FG structure, the initial deformation also features planar dislocation slip (Fig. 12a). At a tensile strain of ~3 %, disordered entanglements around grain boundary and random dislocation distribution in grain interior are observed (Figs. 12b), while strong pile-ups, nanoscale phase transformation and relative clean grain interior that is typically in the FG zone of heterostructure (Figs. 5c& 6) do not appear at all. At large-strain stage (Fig. 12c), dislocation density increases significantly and deformation twinning is activated, leading to steady strain hardening (the blue data in Fig. 4c). However, nanotwin density is obviously lower than that in the FG zone of heterostructure (Fig. 8c, Figs. 8a-b versus Fig. 12c). Great efforts have also made to search for 9R structure and hcp phase near deformation twins at the large-strain stage, but there is no significant phase transformation except for occasional appearance of little hint near triple junctions (Figs. 12c-d). This indicates that the internal stress is not high enough to activate phase transformation.

A freestanding NS material is susceptible to local plastic instability even if it occurs at microscale [83,85]. It has been observed that multiple SBs embryos can nucleate soon after yielding in a homogeneous NS counterpart under tension [28]. However, such embryos are mechanically unstable because work hardening cannot offset the geometrically softening. As a result, individual thriving embryos can readily reap the priority to coalesce and then propagate through the cross-section, thereby dominating global necking instability [3]. Such a strain path is completely supplanted by dispersive stable strain banding in the NS zone of heterostructure (Fig. 10).

4. Discussion

The above comparisons in deformed microstructure reveal the potential deformation mechanisms evoked by hetero-zone interaction, including the intensive pile-ups against HBs, strengthened grain interior, 9R phase transformation near pile-ups, twin/hcp lamella structure and enhanced deformation twinning in FG zone and the dispersed stable SBs in NS zone. Undoubtedly, the high internal stress produced by pile-ups and strengthened FG interior are responsible for the extra yield strength, while the potential phase transformation in FG zone and enhanced twinning in both FG and NG zones are associated with the extra strain hardening (Figs. 4a1, b1 & c). Meanwhile, dispersed SBs enable the heterogeneous microstructure to achieve delocalized strain accommodation at zone scale, which represents another indispensable physics behind the delayed instability of heterostructure. These observations suggest that high long-range internal stress mechanism alone, i.e., high hetero-deformation induced stress [6,86], cannot fully explain the exceptional strength-ductility synergy, particularly as considering the extraordinary work hardening and ductility. While, as discussed next, the high long-range internal stress serves as a necessary or influencing factor for the activation of other potential mechanisms.

4.1. Hetero-zone interaction induced high long-range internal stress

Microstructure heterogeneities result in dramatic difference in the elastic limit between recrystallized FG zone and retained NS zone (Figs. 2a& 4a1). In the elastic-plastic transition stage of tension, micro yielding starts first in the near-HB region of FG zone, since the triaxial stress state resulted from elastic/plastic interaction between zones helps to activate slips near HB [87-89]. At this stage, HBs act as elastic/plastic boundaries, which are impenetrable for gliding dislocations [90], leading to the formation of dislocation pile-ups against them to accommodate the plastic strain difference between zones. Dislocations in pile-up accumulate progressively with applied stress, until the stress concentration at the head is high enough to yield the boundary, i.e.,

attaining the critical state enabling slip transfer or activating sources in the NS side. The limit of pile-up length is thus governed primarily by boundary strength. In a mean-field sense, hetero-zone boundary, such as phase boundary, is generally much stronger than grain boundary in terms of dislocation-dominated yielding [66,91]. Therefore, much stronger pile-ups are expected at HBs (Figs. 5& 6a).

The length of pile-ups against a HB (l_{pileup}) physically represents the effective range of its affected region (l_{Hbar}). Considering the yielding scenario of the hard zone on another side of HB, Chou et al. derived it as a function of the yield strength of constituent zones $l_{pileup} = \left[1-\left(\frac{\sigma_{y,soft}}{\sigma_{y,hard}}\right)^2\right] d_{soft}$ [92]. $\sigma_{y,soft}$, $\sigma_{y,hard}$ and d_{soft} are the yield strength of soft zone, the yield strength of hard zone and the grain size of soft zone, respectively. Employing the k_{HP} in classical Hall-Patch relation as a parameter scaling boundary strength, and concurrently taking into account the stress concentration effect of a pile-up acting on boundary and the back stress acting on Frank-Read source, Wang et al. derived an expression as $l_{pileup} \approx \frac{k_{HP}R^{3/2}}{\sqrt{2}M\mu b}$ [43]. μ, b, M, R represent shear modulus, the magnitude of burgers vector, Taylor factor, and length of the pinning points of source, respectively. Both expressions predict that larger l_{pileup} is associated with stronger HB and higher mechanical incompatibility across HB, and it is on the order of a few micrometers or sub-micrometers for most common HBs. Since the derivation of these expressions incorporates numerous assumptions, here the average length of pile-ups observed experimentally in the strain stage of ~1.5 %−3 %, $\bar{l}_{pileup} \approx 0.72\ \mu m$, is taken to represent the l_{Hbar} of current HBs.

Given that the spacing of HBs is generally several to tens of times greater than $\bar{l}_{pileup}$, the pile-up against an HB is considered to be single-ended. As illustrated in Fig. 13a, in the slip plane forming a mature pile-up from an intragranular Frank-Read source, the accumulated shear plastic strain decreases gradually from γ_0^p at the source to 0 at pile-up tip, and γ_0^p can be calculated based on the continuum dislocation pile-up theory as [67,93]

$$\gamma_0^p = \int_0^{\bar{l}_{pileup}} b(\bar{l}_{pileup}-x)f(x)dx = \frac{3\pi(1-\nu)\tau_{r,FG}\bar{l}_{pileup}^2}{4\mu}, \tag{1}$$

where $f(x) = \frac{2(1-\nu)\tau_{r,FG}}{\mu b}\left(\frac{\bar{l}_{pileup}-x}{x}\right)^{1/2}$, $\tau_{r,FG}$ is the applied stress resolved on the slip plane. This indicates that a pile-up is capable of accommodating a plastic strain difference of magnitude γ_0^p across the HB. Importantly, the yielding of local HB driven by dislocation pile-up also signifies the end of the elastic deformation of NS zone on another side. At this critical state, the total plastic strain difference γ_{total}^p across the HB is

$$\gamma_{total}^p = \frac{\tau_{y,NS}-\tau_{y,FG}}{\mu}, \tag{2}$$

where $\tau_{y,NS}$ and $\tau_{y,FG}$ represent the yield strength of NS zone and FG zone, respectively. Therefore, the density of pile-ups needed to accommodate the deformation incompatibility at the end of elastic-plastic transition is

$$\rho_{pileup} = \frac{\gamma_{total}^p}{\gamma_0^p} = \frac{4\left(\tau_{y,NS}-\tau_{y,FG}\right)}{3\pi(1-\nu)\tau_{r,FG}\bar{l}_{pileup}^2}. \tag{3}$$

The $\tau_{r,FG}$ can be approximated by $\tau_{r,FG} \approx \tau_{y,FG} - \tau_0$, where τ_0 is the friction stress, if one ignores the work hardening of FG zone in this short period. Thus, one obtains

$$\rho_{pileup} \approx \frac{4\left(\tau_{y,NS}-\tau_{y,FG}\right)}{3\pi(1-\nu)\left(\tau_{y,FG}-\tau_0\right)\bar{l}_{pileup}^2}. \tag{4}$$

The τ_0 of $Al_{0.1}CoCrFeNi$ alloy at 77 K obtained by fitting the Hall-Patch relationship is ~60 MPa. Substituting the experimentally measured yield strengths into Eq. (4), the density of pile-ups against the HBs in current heterostructure near global yielding state is estimated to be $\rho_{pileup} \sim 0.8\ \mu m^{-1}$. This indicates that in a 1D simplified configuration along the HB, on average a GND pile-up is needed every 1.25 μm to accommodate the plastic strain discrepancy between zones. It should be noted that the dimension of Eq. (1) appears inconsistent with strain, and that of Eqs. (3-4) appears not μm^{-1}. Such phenomenological discrepancy arises because the integrand in Eq. (1) omits a denominator that should be $1 \times 1\ \mu m^2$ [93,94].

Considering a practical HB at the end of elastic-plastic transition, therefore, there should be multiple pile-ups in an average spacing of $1/\rho_{pileup}$ and an average length of $\bar{l}_{pileup}$. Assuming a simplified 2D scenario with the favored slip planes being perpendicular to the HB ($\boldsymbol{b}//x$) and the dislocations in different slip planes cannot affect the equilibrium position of each other, the pile-ups is illustrated in Fig. 13a. Note that non-uniform pile-up length is caused by local strength variation of HB. The distribution of long-range internal stress $\tau_{long-range}$ thus can be obtained by integrating the interaction of all piling-up dislocations [95]

$$\tau_{long-range}(x,y) = \sum_{j=1}^{n_{pileup}}\sum_{i=1}^{n_{dis}} \tau_{xy}\left(x_i-x, y_j-y\right), \tag{5}$$

where n_{pileup} and n_{dis} are the number of pile-ups and the number of dislocations in the j^{th} pile-up, respectively. $\tau_{xy}(x,y)$ represents the internal stress acting at (x,y) of a dislocation located at (0,0), which is given by [96]

$$\tau_{xy}(x,y) = \frac{\mu b}{2\pi(1-\nu)}\frac{x(x^2-y^2)}{(x^2+y^2)^2} \tag{6}$$

if one assumes that only the shear stress component acting on the slip plane could effectively interact with mobile dislocations [97]. Fig. 13b shows the distribution of $\tau_{long-range}$ in the FG zone. Obviously, except for the oblique sections adjacent to pile-up tip, the direction of $\tau_{long-range}$ acting on the majority of FG zone is opposite to that of the applied stress $\tau_{r,FG}$, thereby serving as back stress for strengthening. Attention must be given to the fact that on the slip plane, the $\tau_{long-range}$ within the piling-up region necessarily balances the $\tau_{r,FG}$, i.e., $\tau_{long-range} = -\tau_{r,FG}$, so as to maintain the equilibrium of dislocations [67]. The $\tau_{long-range}$ acting on the slip planes as a function of distance from HB is plotted in Fig. 13c. Intriguingly, although the $\tau_{long-range}/|\tau_{r,FG}|$ decreases from 1 to ~0.2 within $(0, 2\bar{l}_{pileup})$, the attenuation becomes extremely gradual with further increase the distance from HB. For instance, at a distance of $10\bar{l}_{pileup}$ from the HB, the $\tau_{long-range}/|\tau_{r,FG}|$ remains as high as ~0.2. These establish that, at the critical state of global yielding of heterostructure, the flow stress of FG zone is enhanced by ~20 %, at least within regions $<10\bar{l}_{pileup}$ from the HB. This micro-mechanics is responsible for the relatively clean interior of FGs near HB at the low strain stage (Figs. 5& 6a).

Conjugate to the back stress in the FG zone, pile-ups also causes forward stress in the NS zone, which facilitates local yielding. However, the coupling of back stress and forward stress is not a zero-sum game [6, 86]; for integrated heterostructure, the 'weakening effect' of forward stress cannot completely offsets the strengthening effect of back stress [14,15]. These are the primary physics why the experimentally observed extra strengthening of global heterostructure ($\sigma_{y,extra}$ accounting for ~9 % of total yield strength, Figs. 4a1 & b1) is lower than the strengthening magnitude of its FG zone (~20 %). Note that pile-ups also contribute to Tylor strengthening, but here this effect is believed to be insignificant since dislocation density is not very high at the yielding stage.

4.2. Unusual phase transformation evoked by long-range internal stress

When the stress exceeds the threshold, the 9R structure and the

severely deformed fcc matrix can transform, via slipping through two atomic layers of adjacent SFs under stress, to hcp phase [98,99]. In other words, the martensitic transformation may proceed via either fcc→9R→hcp path or fcc→hcp path, or both paths simultaneously [70, 100]. For the current heterostructure, the detection of 9R at early plastic stage (Fig. 6) and the coexistence of 9R and hcp phase at the large strain stage (Fig. 7) imply that all these paths are possible. For any possible case, the stress initiating phase transformation (τ_{TRIP}) can be represented by the critical stress for the growth of hcp nucleus. Therefore, following the nucleation model of hcp-martensite primarily proposed by Mahajan et al. [101], which involves the activity of Shockley partials on every second {111} plane, the τ_{TRIP} of FG zone can be conservatively estimated by [102,103]

$$\tau_{TRIP} = \frac{2E^{fcc/hcp}}{3b_p} + \frac{3\mu b_p}{L_{tr}} + \frac{h\Delta G^{fcc\to hcp}}{3b_p}, \tag{8}$$

if ignoring the dependence on grain size so as to avoid the difficulties posed by uncertain empirical parameters. b_p (~0.144 nm) is the magnitude of the burgers vector of Shockley partial [38]. L_{tr} represents the length of the sessile partials forming a hcp nucleus, which logically must not exceed the characteristic length of the early martensite embryo, estimated at an average value of ~80 nm based on experimental observations such as that in Fig. 6a [102]. h (~$5a/\sqrt{3}$ ≈1.02 nm) is the thickness of hcp nucleus [101]. $\Delta G^{fcc\to hcp}$ is the change in Gibbs free energy per unit volume occurring fcc→hcp transformation, approximated here as about −30 mJ/mm^3 based on the calculation for $Al_{0.3}CoCrFeNi$ using density functional perturbation theory, corresponding to about −200 J/mol [36]. $E^{fcc/hcp}$ denotes the fcc/hcp interface energy per unit area, which is thermodynamically associated with stacking fault energy Γ_{sf} as $\Gamma_{sf} = 2E^{fcc/hcp} + 2\rho\Delta G^{fcc\to hcp}$, where $\rho = 3.06\times10^{-11}$ $mol{\cdot}mm^{-2}$ represents the molar surface density along {111} plane [104]. $E^{fcc/hcp}$ is thereof calculated to be 13.2 mJ/m^2.

Substituting the parameters into Eq. (8) yields τ_{TRIP} ≈ 460 MPa. It is much higher than the applied stress in a homogeneous FG counterpart near yielding ($\tau_{r,FG}$ ≈ 250 MPa). Interestingly, soon after yielding, this critical stress is attainable in the near-HB region of FG zone in a heterostructure, where local resolved internal stress $\tau_{r,local}$ is increased by back stress to $\tau_{r,\ local} = \tau_{r,FG} + |\tau_{long-range}|$. Adjacent to the tail of dislocation pile-ups, $\tau_{r,local}$ approaches $2\tau_{r,FG}$ (~500 MPa, Fig. 13c), yet with a low density of mobile defects (Figs. 5& 6a), phase transformation is thereby evoked. These findings demonstrate a deformation fundamental of heterostructure: in addition to directly increasing strength, the long-range internal stress induced by dislocation pile-ups can assist in invoking hard plastic mechanisms that are difficult to activate in a freestanding constituent, such as fcc→hcp phase transformation.

Similar to the effect on phase transition, the high internal stress caused by back stress can also facilitate twinning (Fig. 8c). Enhanced transformation and twinning accommodate the applied strain, and at the same time serve as additional obstacles or sources for dislocation slip, leading to extra work hardening (Fig. 4c).

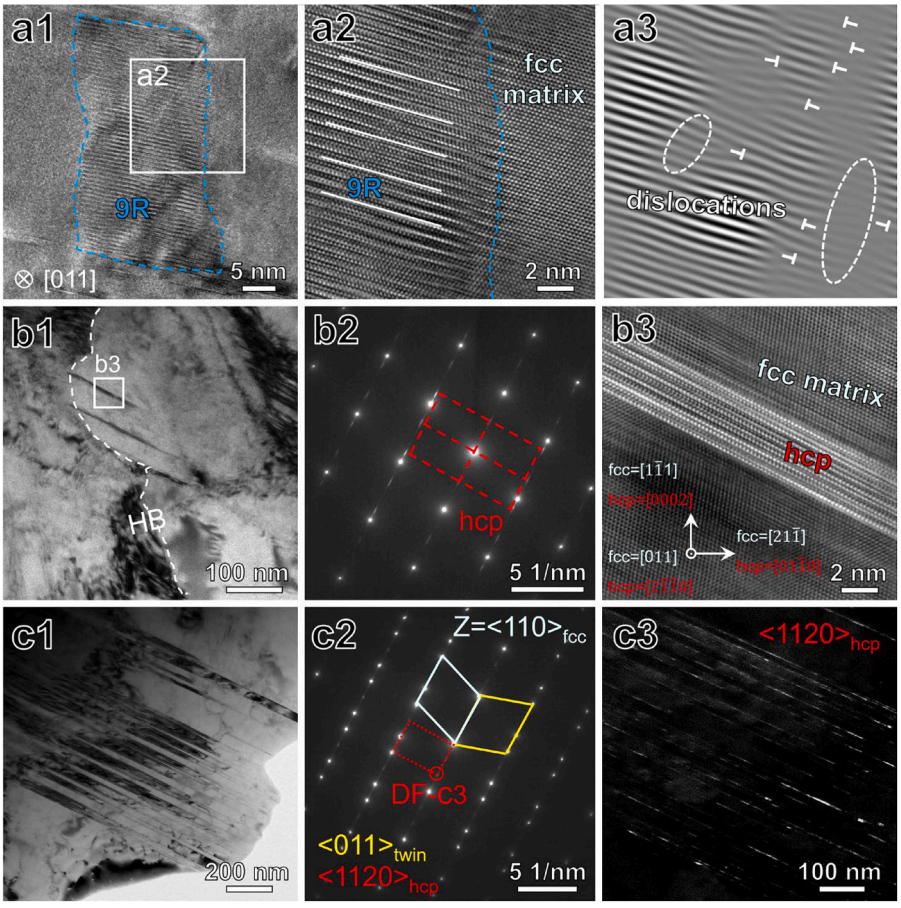

Fig. 7. Representative TEM images showing (a) extensive 9R phase formation and (b, c) well-developed nano-layer hcp phases in the FG zone at ~20 % tensile strain at 77 K. (a2) Magnified image of the interface between 9R and fcc phases; (a3) inverse-FFT (IFFT) pattern of the 9R/fcc interface region. (b1) Bright-field TEM image showing the hcp phase in the vicinity of HB. The corresponding selected area electron diffraction (SAED) pattern and lattice images are given in (b2, b3). (c2) The SAED pattern in (c1) confirm the coexistence of fcc matrix, twins and hcp phases. (c3) Dark-field TEM image obtained using the {0001} diffraction plane to highlight the thin hcp laths.

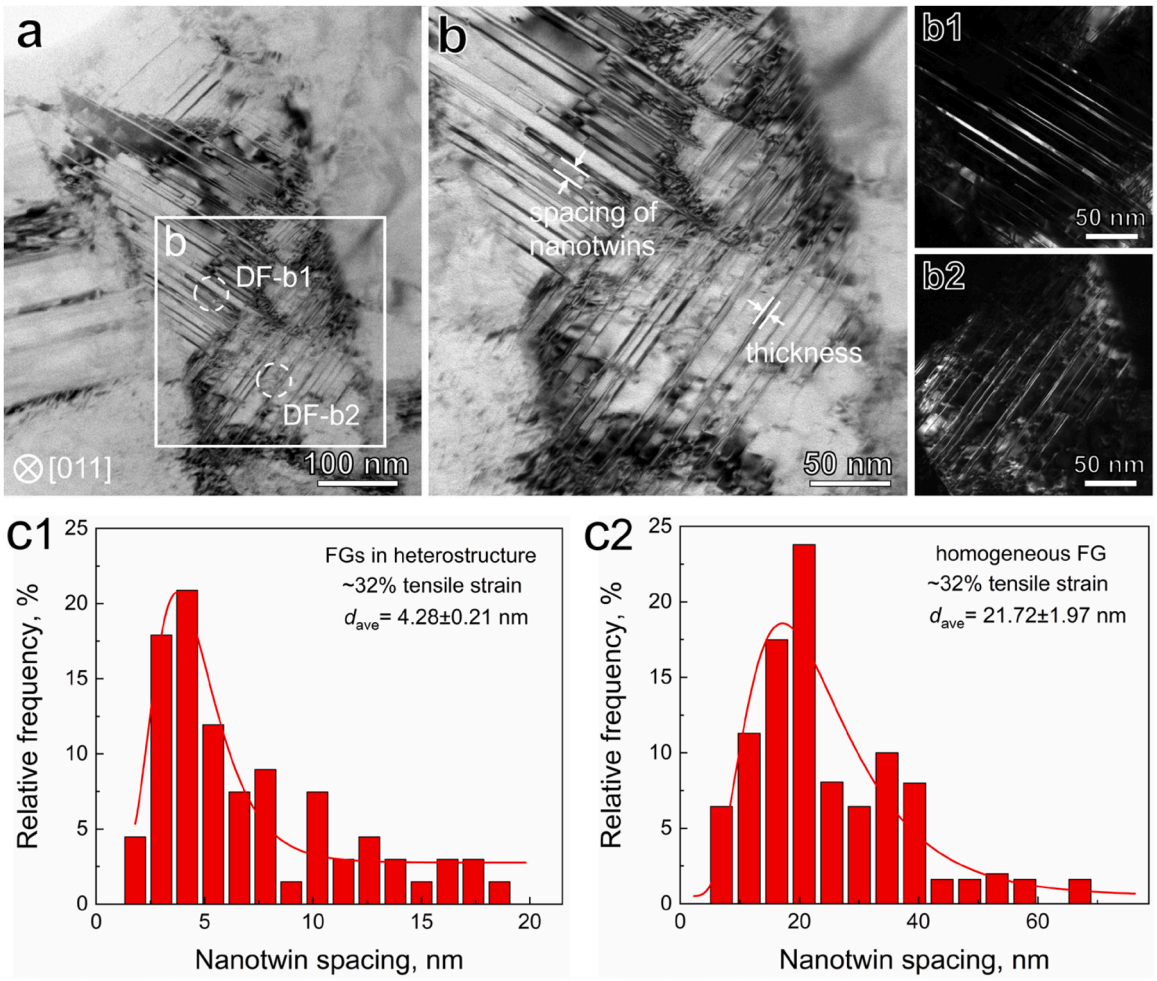

Fig. 8. Enhanced deformation twinning in the FG zone of heterostructure at the large-strain stage (~32 % tensile strain) at 77 K. (a, b) Bright-field TEM images showing high-density deformation twins in thickness of a few nanometers. (b1) and (b2) Dark-field TEM images obtained using the {111} diffraction plane to highlight the nanotwins with different orientations. Statistical distribution of nanotwins spacing compared between (c1) the FG zone in heterostructure and (c2) homogeneous FG with comparable applied strain.

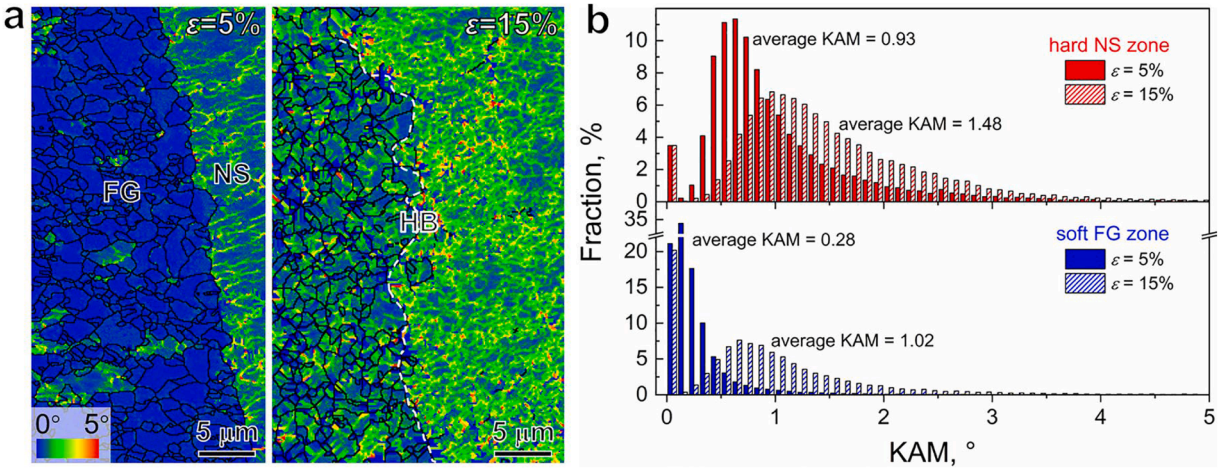

Fig. 9. Deformation of the NS zone in heterostructure at 77 K. The (a) map and (b) statistical distribution of kernel average misorientation (KAM) across HB with increasing strain. The decent increase of KAM in NS zone proves that it becomes ductile under the constraint from FG neighbors.

4.3. Formation of dispersed stable SBs evoked by hetero-zone interaction

Upon entering the yielding stage, strain incompatibility-induced inter-zone constraint transfers load from FG matrix to NS lamella, as resolved by the shear-lag model [105,106]. Meanwhile, dislocation pile-ups in the FG side enhances the internal stress of NS zone, especially

in the vicinity of HB [95]. Once the applied stress in NS zone attains the yield strength, micro plastic instability can be readily activated from the sites with higher distortion energy to alleviate local stress concentration, leading to the nucleation of early SB embryos [28]. This occurs because the limited work hardening of NS zone cannot offset local geometrical softening under mechanical perturbation [107,108]. As the early SBs propagate to approach an HB, increased dislocation activity and constraint from FG neighbor play roles in relieving stresses at their tips [109], thereby arresting the propagating SBs (Fig. 10). The lamella configuration of NS zone (Fig. 1a) can significantly enhance such arresting effect, since it imparts high-density HBs to confine the free propagation path, particularly in the direction of zone thickness. Arrested early SBs enables the formation of new stress concentration sites in the virginal region, providing the opportunity to nucleate more SBs until they dispersed over the whole NS zone (Fig. 10). This is the formation physics of dispersed SBs.

In the stable plastic flow stage, the strain concentration intensity (I) of SBs gradually increases, while their characteristic width (W) remains nearly unchanged (Fig. 14a). Although there are indeed some intensity variations among SBs, they develop side by side, with the advanced ones wait for the lagging ones and no unstable coalescence (Fig. 14b). In addition to the arresting effect from FG neighbor, work hardening by twinning and dislocations activity (Fig. 11) in SBs should also contribute to their stable evolution. Stabilized SBs ensure the entire NS zone maintains high stress, which not only endows the NS zone with persistent load-bearing capability but also allows the non-strain banding region to share a portion of applied strain (Fig. 14a) [28,81].

In other words, limited strain hardening capability, microstructure heterogeneity and the resulting inter-zone constraint are the two necessary conditions for activating dispersed stable SBs in NS zone. The former renders the nucleation of SBs by local plastic instability, which is generally intrinsic to a NS zone. The latter plays the key role in stabilizing SBs and thus ensuring dispersed nucleation. Dispersed SBs and their stable evolution endow exceptional trans-scale mechanical effects. First, the NS zone itself exhibits notable strain accommodation capability, and its strain path and stress-strain response are thus dramatically altered compared to those of the freestanding counterpart [81]. Second, at the zone scale, the inter-zone deformation compatibility is significantly enhanced, with the strain partitioned into NS zone exceeding 85 % of that in FG zone (Fig. 14c). Moreover, these leads to the integrated heterostructure displaying improved uniform elongation under high flow stress.

The above discussions highlighted the mechanical principle of the formation of dispersed SBs. Estrin et al. suggested that the crystallographic mechanism, which may be related to the dislocation pile-up induced forward stress, is critical as well [110]. However, Ma et al. asserted that the long-range internal stress is not the primary cause because the feature size of SBs in layered/gradient heterostructure are

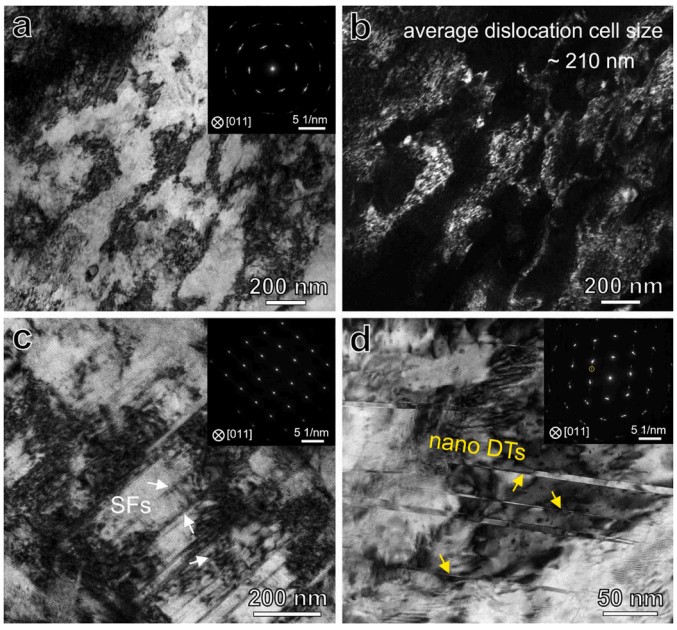

Fig. 11. Representative TEM images comparing the microstructure of the non-recrystallized NS zone (a, b) before and (c, d) after tension at 77 K. The formation of (c) SFs and (d) deformation twins are observed in the NS zone after ~5 % and ~15.5 % tensile strain, respectively, proved by SAED patterns.

commensurate with the macroscopic sample size [107]. This assertion clearly overlooks the fact that in many heterostructures, such as the current lamella structure (Fig. 10), heterogeneous laminates [81], bimodal structure [111] and conventional dual steels [112], the characteristic width of SBs is either smaller than zone dimension or exactly on the same order. These deserves more systematic investigation.

5. Summary

In summary, with the challenges in understanding the synergistic mechanical effects and underlying mechanisms of heterostructured materials, here we particularly focused on how long-range internal stress interact with other mechanisms and how hetero-zone interaction affect strain accommodation. The deformation responses and trans-scale mechanisms of a heterostructure in $Al_{0.1}CoCrFeNi$ alloy, composed of NS lamella embedded in FG matrix with dense HBs, is studied, by combining experimental observations and theoretical analyses. Specifically, the main findings are:

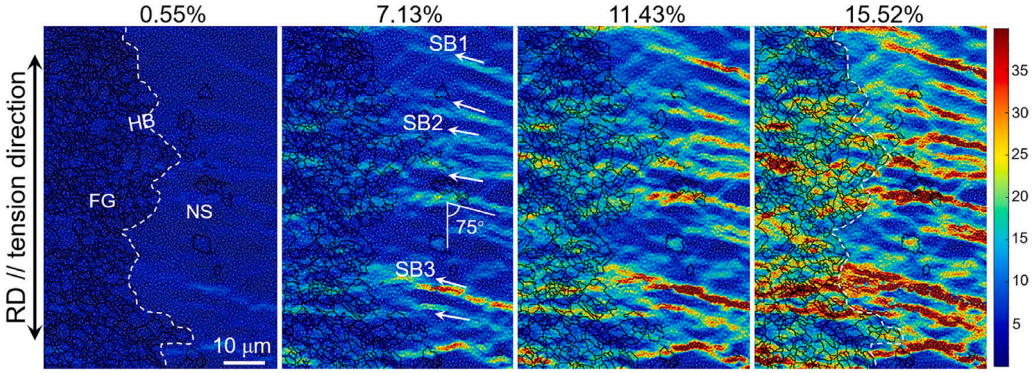

Fig. 10. Abnormal strain accommodation mechanism of the non-recrystallized NS zone, by forming dispersed stable strain bands, unveiled by the micro strain mapping (the strain component along tension direction) across HB at 77 K. The number above each subgraph represents the applied strain.

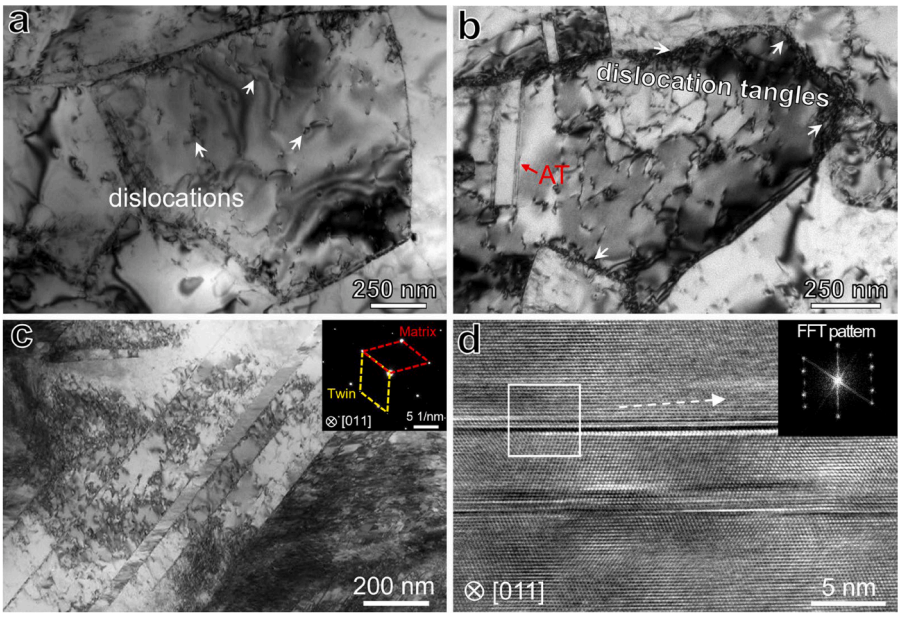

Fig. 12. Deformation of homogeneous FG at 77 K. (a) TEM image showing the planar dislocation activity at ~1 % tensile strain. (b) TEM image showing the dislocation tangles near grain boundaries and random dislocation activity in grain interior, at ~3 % tensile strain. (c) Bright-field STEM image of the typical deformation nanotwins with tangled dislocations at ~32 % tensile strain. (d) Representative high-resolution TEM image and FFT pattern in the region with relatively complex deformation.

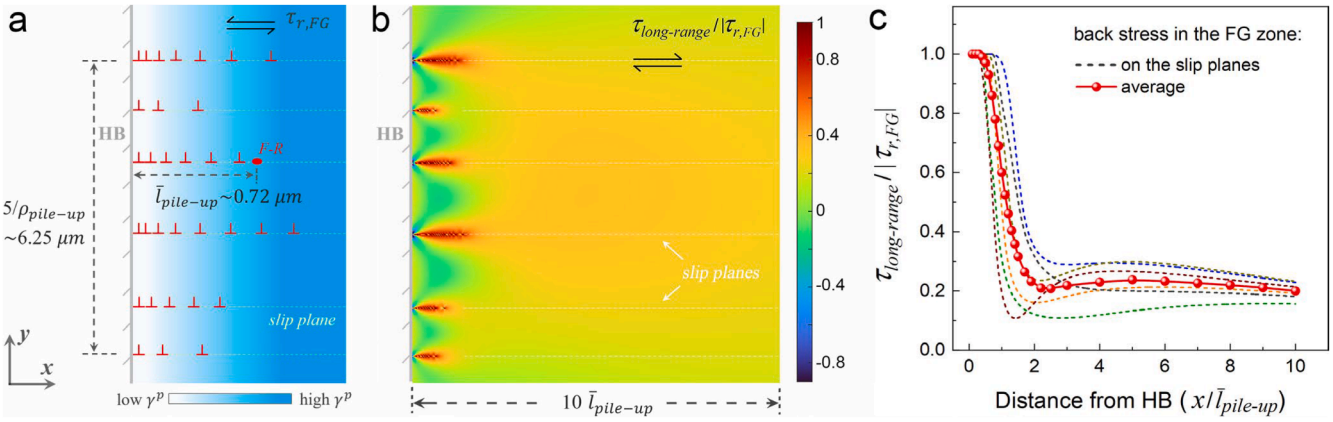

Fig. 13. (a) Schematic diagram of dislocation pile-ups against an HB to accommodate the plastic strain gradient in FG zone, at the end of elastic-plastic transition. (b) The map of long-range internal stress induced by the pile-ups (back stress in the FG side, $\tau_{long-range}/|\tau_{r,FG}|$). (c) Linear distribution of long-range internal stress on the slip planes, plotted as a function of distance from HB.

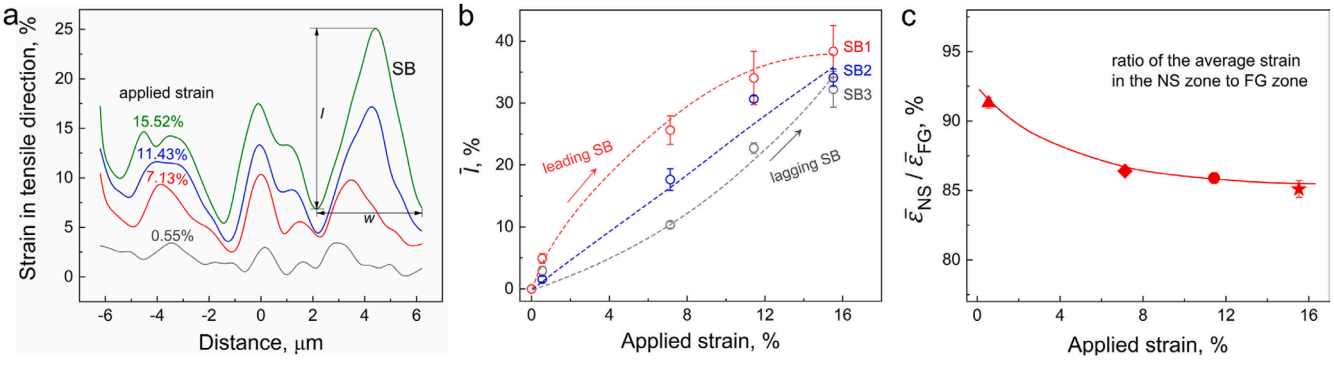

Fig. 14. Evolution and the strain accommodation effects of dispersed SBs in the NS zone of heterostructure. (a) Statistically averaged distribution of tensile strain cross SBs, illustrating the definition of the strain concentration intensity (I) and characteristic width (W) of SBs. (b) Evolution of I in three typical SBs with different development rate (indicated by white arrows in Fig. 10). (c) Strain partitioning indexed by the ratio $\bar{\varepsilon}_{NS}/\bar{\varepsilon}_{FG}$ as a function of applied strain, where $\bar{\varepsilon}_{NS}$ and $\bar{\varepsilon}_{FG}$ represent the average strain of NS zone and FG zone, respectively.

(i) At the yielding stage, elastoplastic interaction between zones renders the accumulation of strong dislocation pile-ups against HBs, with an average length ($\bar{l}_{pileup}$) of up to ~0.72 μm and a density of ~0.8 μm^{-1}. This generates high back stress in FG zone, nearly doubling the internal stress of dislocation piling region, and increasing the internal stress by ~20 % in the region even $10\bar{l}_{pileup}$ away from the HB. Such strengthening effect is partially offset by the forward stress, yielding an extra strengthening accounting for ~9 % of the yield strength.

(ii) Benefiting from the high long-range internal stress, the critical phase transformation stress of FG zone is attainable, leading to the activation of 9R transformation initially in the vicinity of pile-up tail soon after yielding and nanolayered hcp transformation at the large-strain stage. Meanwhile, improved internal stress also enhances twinning. These mechanisms result in extra work hardening.

(iii) Hetero-zone interaction activates dispersed stable SBs in the NS zone, which promotes delocalized strain partitioning between zones and thus improves uniform elongation. Limited strain hardening capability renders SBs nucleation, while inter-zone constraint plays the key role in stabilizing SBs and thus ensuring dispersed nucleation.

(iv) Phase transformation and dispersed stable SBs cannot be activated in homogeneous materials. A deformation fundamental for heterostructure is thus elucidated: beyond directly contributing to strength, hetero-zone interaction and the development of long-range internal stress could assist in invoking extra hard plastic mechanisms otherwise inaccessible to the homogeneous counterparts.

CRediT authorship contribution statement

Jiahao Li: Writing – original draft, Formal analysis. **Xinkai Ma:** Writing – review & editing, Supervision, Funding acquisition, Formal analysis. **Kejie Lu:** Data curation. **Yanfei Wang:** Writing – review & editing, Formal analysis. **Yuntian Zhu:** Writing – review & editing.

Declaration of competing interest

The authors declare that they have no known competing financial interests or personal relationships that could have appeared to influence the work reported in this paper.

Acknowledgments

This work was supported by the National Natural Science Foundation of China (Grant Nos. 52201142, 12102006, 12472109 and 51931003), the Hong Kong Research Grants Council (GRF 11214121) and the Fundamental Research Funds for the Central Universities (Grant No. 2682024GF014). We also would like to thank the Analytical and Testing Center of Southwest Jiaotong University for TEM characterization.

References

[1] D. Raabe, C.C. Tasan, E.A. Olivetti, Strategies for improving the sustainability of structural metals, Nature 575 (7781) (2019) 64–74.
[2] R.O. Ritchie, The conflicts between strength and toughness, Nat. Mater. 10 (11) (2011) 817–822.
[3] M.A. Meyers, A. Mishra, D.J. Benson, Mechanical properties of nanocrystalline materials, Prog. Mater. Sci. 51 (4) (2006) 427–556.
[4] L. Gu, A. Meng, X. Chen, Y. Zhao, Simultaneously enhancing strength and ductility of HCP titanium via multi-modal grain induced extra< c+ a>dislocation hardening, Acta Mater 252 (2023) 118949.
[5] P. Sathiyamoorthi, H.S. Kim, High-entropy alloys with heterogeneous microstructure: processing and mechanical properties, Prog. Mater. Sci. 123 (2022) 100709.
[6] Y. Zhu, K. Ameyama, P.M. Anderson, I.J. Beyerlein, H. Gao, H.S. Kim, E. Lavernia, S. Mathaudhu, H. Mughrabi, R.O. Ritchie, Heterostructured materials: superior properties from hetero-zone interaction, Mater. Res. Lett. 9 (1) (2021) 1–31.
[7] Y. Zhu, X. Wu, Heterostructured materials, Prog. Mater. Sci. 131 (2023) 101019.
[8] Z. Cheng, H. Zhou, Q. Lu, H. Gao, L. Lu, Extra strengthening and work hardening in gradient nanotwinned metals, Science 362 (6414) (2018) eaau1925.
[9] X. Wu, P. Jiang, L. Chen, J. Zhang, F. Yuan, Y. Zhu, Synergetic strengthening by gradient structure, Mater. Res. Lett. 2 (4) (2014) 185–191.
[10] Y. Wang, M. Wang, X. Fang, F. Guo, H. Liu, R. Scattergood, C. Huang, Y. Zhu, Extra strengthening in a coarse/ultrafine grained laminate: Role of gradient interfaces, Int. J. Plast. 123 (2019) 196–207.
[11] Y. Wang, Y. Zhu, Z. Yu, J. Zhao, Y. Wei, Hetero-zone boundary affected region: a primary microstructural factor controlling extra work hardening in heterostructure, Acta Mater 241 (2022) 118395.
[12] G. Li, J. Jiang, H. Ma, R. Zheng, S. Gao, S. Zhao, C. Ma, K. Ameyama, B. Ding, X. Li, Superior strength–ductility synergy in three-dimensional heterogeneous-nanostructured metals, Acta Mater 256 (2023) 119143.
[13] C. Huang, Y. Wang, X. Ma, S. Yin, H. Höppel, M. Göken, X. Wu, H. Gao, Y. Zhu, Interface affected zone for optimal strength and ductility in heterogeneous laminate, Mater. Today 21 (7) (2018) 713–719.
[14] Y. Wang, M. Yang, X. Ma, M. Wang, K. Yin, A. Huang, C. Huang, Improved back stress and synergetic strain hardening in coarse-grain/nanostructure laminates, Mater. Sci. Eng. A 727 (2018) 113–118.
[15] X. Wu, M. Yang, F. Yuan, G. Wu, Y. Wei, X. Huang, Y. Zhu, Heterogeneous lamella structure unites ultrafine-grain strength with coarse-grain ductility, Proc. Natl. Acad. Sci. 112 (47) (2015) 14501–14505.
[16] M. Huang, C. Xu, G. Fan, E. Maawad, W. Gan, L. Geng, F. Lin, G. Tang, H. Wu, Y. Du, Role of layered structure in ductility improvement of layered Ti-Al metal composite, Acta Mater 153 (2018) 235–249.
[17] P. Shi, Y. Zhong, Y. Li, W. Ren, T. Zheng, Z. Shen, B. Yang, J. Peng, P. Hu, Y. Zhang, Multistage work hardening assisted by multi-type twinning in ultrafine-grained heterostructural eutectic high-entropy alloys, Mater. Today 41 (2020) 62–71.
[18] Y. Wang, X. Ma, F. Guo, Z. Zhao, C. Huang, Y. Zhu, Y. Wei, Strong and ductile CrCoNi medium-entropy alloy via dispersed heterostructure, Mater. Design 225 (2023) 111593.
[19] K. Jiang, T. Ren, G. Shan, T. Ye, L. Chen, C. Wang, F. Zhao, J. Li, T. Suo, Dynamic mechanical responses of the $Al_{0.1}$CoCrFeNi high entropy alloy at cryogenic temperature, Mater. Sci. Eng. A 797 (2020) 140125.
[20] Q. Li, T. Zhang, J. Qiao, S. Ma, D. Zhao, P. Lu, Z. Wang, Mechanical properties and deformation behavior of dual-phase $Al_{0.6}$CoCrFeNi high-entropy alloys with heterogeneous structure at room and cryogenic temperatures, J. Alloys Compd. 816 (2020) 152663.
[21] D. Liu, X. Jin, N. Guo, P. Liaw, J. Qiao, Non-equiatomic FeMnCrNiAl high-entropy alloys with heterogeneous structures for strength and ductility combination, Mater. Sci. Eng. A 818 (2021) 141386.
[22] M. Yang, D. Yan, F. Yuan, P. Jiang, E. Ma, X. Wu, Dynamically reinforced heterogeneous grain structure prolongs ductility in a medium-entropy alloy with gigapascal yield strength, Proc. Natl. Acad. Sci 115 (28) (2018) 7224–7229.
[23] S. Guo, Z. Ma, G. Xia, X. Li, Z. Xu, W. Li, X. Jin, X. Cheng, Pursuing ultrastrong and ductile medium entropy alloys via architecting nanoprecipitates-enhanced hierarchical heterostructure, Acta Mater 263 (2024) 119492.
[24] X. Wu, Y. Zhu, Heterogeneous materials: a new class of materials with unprecedented mechanical properties, Mater. Res. Lett. 5 (8) (2017) 527–532.
[25] J. Zhao, M. Zaiser, X. Lu, B. Zhang, C. Huang, G. Kang, X. Zhang, Size-dependent plasticity of hetero-structured laminates: a constitutive model considering deformation heterogeneities, Int. J. Plast. 145 (2021) 103063.
[26] C.C. Tasan, M. Diehl, D. Yan, C. Zambaldi, P. Shanthraj, F. Roters, D. Raabe, Integrated experimental–simulation analysis of stress and strain partitioning in multiphase alloys, Acta Mater 81 (2014) 386–400.
[27] F. He, Z. Yang, S. Liu, D. Chen, W. Lin, T. Yang, D. Wei, Z. Wang, J. Wang, J.j. Kai, Strain partitioning enables excellent tensile ductility in precipitated heterogeneous high-entropy alloys with gigapascal yield strength, Int. J. Plast. 144 (2021) 103022.
[28] Y. Wang, Y. Zhu, Y. Wei, C. Huang, Inter-zone constraint modifies the stress-strain response of the constituent layer in gradient structure, Sci. China Mater. 64 (2021) 3114–3123.
[29] E. Ma, T. Zhu, Towards strength–ductility synergy through the design of heterogeneous nanostructures in metals, Mater. Today 20 (6) (2017) 323–331.
[30] J. Li, W. Lu, S. Chen, C. Liu, Revealing extra strengthening and strain hardening in heterogeneous two-phase nanostructures, Int. J. Plast. 126 (2020) 102626.
[31] J. Zhao, X. Lu, F. Yuan, Q. Kan, S. Qu, G. Kang, X. Zhang, Multiple mechanism based constitutive modeling of gradient nanograined material, Int. J. Plast. 125 (2020) 314–330.
[32] F. Xiong, Y. Wu, X. Liu, H. Wang, S. Jiang, X. Zhang, Z. Lu, Enhancing cryogenic yield strength and ductility of the Al0. 1CoCrFeNi high-entropy alloy by synergistic effect of nanotwins and dislocations, Scr. Mater. 232 (2023) 115495.
[33] S. Wu, G. Wang, Q. Wang, Y. Jia, J. Yi, Q. Zhai, J. Liu, B. Sun, H. Chu, J. Shen, Enhancement of strength-ductility trade-off in a high-entropy alloy through a heterogeneous structure, Acta Mater 165 (2019) 444–458.
[34] S. Wu, G. Wang, J. Yi, Y. Jia, I. Hussain, Q. Zhai, P. Liaw, Strong grain-size effect on deformation twinning of an Al0. 1CoCrFeNi high-entropy alloy, Mater. Res. Lett. 5 (4) (2017) 276–283.
[35] Q. Pan, M. Yang, R. Feng, A.C. Chuang, K. An, P.K. Liaw, X. Wu, N. Tao, L. Lu, Atomic faulting induced exceptional cryogenic strain hardening in gradient cell–structured alloy, Science 382 (6667) (2023) 185–190.
[36] Y. Zhu, X. Wu, Perspective on hetero-deformation induced (HDI) hardening and back stress, Mater. Res. Lett. 7 (10) (2019) 393–398.

[37] G. Chen, J. Qiao, Z. Jiao, D. Zhao, T. Zhang, S. Ma, Z. Wang, Strength-ductility synergy of Al0. 1CoCrFeNi high-entropy alloys with gradient hierarchical structures, Scr. Mater. 167 (2019) 95–100.

[38] X. Xu, P. Liu, Z. Tang, A. Hirata, S. Song, T. Nieh, P. Liaw, C. Liu, M. Chen, Transmission electron microscopy characterization of dislocation structure in a face-centered cubic high-entropy alloy $Al_{0.1}$CoCrFeNi, Acta Mater 144 (2018) 107–115.

[39] C. Liang, Q. Zhang, Y. Shao, Y. Bu, J. Liu, X. Li, H. Wang, W. Yang, Influence of load orientations with respect to twin boundaries on the deformation behaviors of high-entropy alloy nanocrystals, MRS Bull 46 (2021) 205–216.

[40] K. Jiang, Q. Zhang, J. Li, X. Li, F. Zhao, B. Hou, T. Suo, Abnormal hardening and amorphization in an FCC high entropy alloy under extreme uniaxial tension, Int. J. Plast. 159 (2022) 103463.

[41] A. Saeed-Akbari, J. Imlau, U. Prahl, W. Bleck, Derivation and variation in composition-dependent stacking fault energy maps based on subregular solution model in high-manganese steels, Metall. Mater. Trans. A 40 (2009) 3076–3090.

[42] Z. Cheng, L. Lu, The effect of gradient order on mechanical behaviors of gradient nanotwinned Cu, Scr. Mater. 164 (2019) 130–134.

[43] Y. Wang, C. Huang, X. Ma, J. Zhao, F. Guo, X. Fang, Y. Zhu, Y. Wei, The optimum grain size for strength-ductility combination in metals, Int. J. Plast. 164 (2023) 103574.

[44] Y. Wang, Y. Wei, Strain energy density maximization principle for material design and the reflection in trans-scale continuum theory, J Mech Phys Solids (2024) 105912.

[45] X. Xu, P. Liu, A. Hirata, S. Song, T. Nieh, M. Chen, Microstructural origins for a strong and ductile Al0. 1CoCrFeNi high-entropy alloy with ultrafine grains, Materialia 4 (2018) 395–405.

[46] J. Yang, J. Qiao, S. Ma, G. Wu, D. Zhao, Z. Wang, Revealing the Hall-Petch relationship of Al0. 1CoCrFeNi high-entropy alloy and its deformation mechanisms, J. Alloys Compd. 795 (2019) 269–274.

[47] J. Hou, J. Qiao, J. Lian, P.K. Liaw, Revealing the relationship between microstructures, textures, and mechanical behaviors of cold-rolled $Al_{0.1}$CoCrFeNi high-entropy alloys, Mater. Sci. Eng. A 804 (2021) 140752.

[48] S. Wu, L. Xu, X. Ma, Y. Jia, Y. Mu, Y. Jia, G. Wang, C. Liu, Effect of annealing temperatures on microstructure and deformation behavior of $Al_{0.1}$CrFeCoNi high-entropy alloy, Mater. Sci. Eng. A 805 (2021) 140523.

[49] J. Li, K. Lu, X. Zhao, X. Ma, F. Li, H. Pan, J. Chen, A superior strength-ductility synergy of $Al_{0.1}$CrFeCoNi high-entropy alloy with fully recrystallized ultrafine grains and annealing twins, J. Mater. Sci. Technol. 131 (2022) 185–194.

[50] F. Otto, A. Dlouhý, C. Somsen, H. Bei, G. Eggeler, E.P. George, The influences of temperature and microstructure on the tensile properties of a CoCrFeMnNi high-entropy alloy, Acta Mater 61 (15) (2013) 5743–5755.

[51] S.K. Vajpai, C. Sawangrat, O. Yamaguchi, O.P. Ciuca, K. Ameyama, Effect of bimodal harmonic structure design on the deformation behaviour and mechanical properties of Co-Cr-Mo alloy, Mater. Sci. Eng. C 58 (2016) 1008–1015.

[52] X. Ma, C. Huang, W. Xu, H. Zhou, X. Wu, Y. Zhu, Strain hardening and ductility in a coarse-grain/nanostructure laminate material, Scr. Mater. 103 (2015) 57–60.

[53] Y. Wang, C. Huang, Z. Li, X. Fang, M. Wang, Q. He, F. Guo, Y. Zhu, Shear band stability and uniform elongation of gradient structured material: Role of lateral constraint, Extrem. Mech. Lett. 37 (2020) 100686.

[54] M. Klimova, D. Shaysultanov, A. Semenyuk, S. Zherebtsov, N. Stepanov, Effect of carbon on recrystallised microstructures and properties of CoCrFeMnNi-type high-entropy alloys, J. Alloys Compd. 851 (2021) 156839.

[55] S.H. Shim, J. Moon, H. Pouraliakbar, B.J. Lee, S.I. Hong, H.S. Kim, Toward excellent tensile properties of nitrogen-doped CoCrFeMnNi high-entropy alloy at room and cryogenic temperatures, J. Alloys Compd. 897 (2022) 163217.

[56] S. Sun, Y. Tian, H. Lin, X. Dong, Y. Wang, Z. Wang, Z. Zhang, Temperature dependence of the Hall–Petch relationship in CoCrFeMnNi high-entropy alloy, J. Alloys Compd. 806 (2019) 992–998.

[57] S. Sun, Y. Tian, H. Lin, H. Yang, X. Dong, Y. Wang, Z. Zhang, Achieving high ductility in the 1.7 GPa grade CoCrFeMnNi high-entropy alloy at 77 K, Mater. Sci. Eng. A 740 (2019) 336–341.

[58] A.S. Tirunilai, J. Sas, K.P. Weiss, H. Chen, D.V. Szabó, S. Schlabach, S. Haas, D. Geissler, J. Freudenberger, M. Heilmaier, Peculiarities of deformation of CoCrFeMnNi at cryogenic temperatures, J. Mater. Res. 33 (19) (2018) 3287–3300.

[59] B. Gludovatz, A. Hohenwarter, K.V. Thurston, H. Bei, Z. Wu, E.P. George, R. O. Ritchie, Exceptional damage-tolerance of a medium-entropy alloy CrCoNi at cryogenic temperatures, Nat. Commun. 7 (1) (2016) 10602.

[60] F. Guo, L. Song, Q. He, B. Yang, X. Zheng, Q. Wang, C. Huang, Enhancing cryogenic tensile properties of CrCoNi medium entropy alloy via heterogeneous microstructure design, Mater. Charact. 201 (2023) 112951.

[61] B. Han, C. Zhang, K. Feng, Z. Li, X. Zhang, Y. Shen, X. Wang, H. Kokawa, R. Li, Z. Wang, Additively manufactured high strength and ductility CrCoNi medium entropy alloy with hierarchical microstructure, Mater. Sci. Eng. A 820 (2021) 141545.

[62] L. Gu, A. Meng, X. Chen, Y. Zhao, Simultaneously enhancing strength and ductility of HCP titanium via multi-modal grain induced extra< c+ a>dislocation hardening, 252 (2023) 118949.

[63] D. Zhang, J. Zhang, J. Kuang, G. Liu, J. Sun, Superior strength-ductility synergy and strain hardenability of Al/Ta co-doped NiCoCr twinned medium entropy alloy for cryogenic applications, Acta Mater 220 (2021) 117288.

[64] Z. Zhang, W. Wang, S. Qin, M. Yang, J. Wang, P. Jiang, F. Yuan, X. Wu, Dual heterogeneous structured medium-entropy alloys showing a superior strength-ductility synergy at cryogenic temperature, J. Mater. Res. Technol. 17 (2022) 3262–3276.

[65] M.I. Latypov, S. Shin, B.C. De Cooman, H.S. Kim, Micromechanical finite element analysis of strain partitioning in multiphase medium manganese TWIP+ TRIP steel, Acta Mater 108 (2016) 219–228.

[66] Y. Liu, M. Xu, L. Xiao, X. Chen, Z. Hu, B. Gao, N. Liang, Y. Zhu, Y. Cao, H. Zhou, Dislocation array reflection enhances strain hardening of a dual-phase heterostructured high-entropy alloy, Mater. Res. Lett. 11 (8) (2023) 638–647.

[67] J.P. Hirth, J. Lothe, Book Theory of Dislocations, Second, John Wiley, USA, 1982.

[68] A. Gouldstone, H.J. Koh, K.Y. Zeng, A. Giannakopoulos, S. Suresh, Discrete and continuous deformation during nanoindentation of thin films, Acta Mater 48 (9) (2000) 2277–2295.

[69] A. Misra, J. Hirth, R. Hoagland, Length-scale-dependent deformation mechanisms in incoherent metallic multilayered composites, Acta Mater 53 (18) (2005) 4817–4824.

[70] L. Wang, S. Xiang, Y. Tan, W. Shi, Y. Cai, X. Ji, The role of 9R structures on deformation-induced martensitic phase transformations in dual-phase high-entropy alloys, Mater. Sci. Eng. A 853 (2022) 143705.

[71] W. Lu, C.H. Liebscher, F. Yan, X. Fang, L. Li, J. Li, W. Guo, G. Dehm, D. Raabe, Z. Li, Interfacial nanophases stabilize nanotwins in high-entropy alloys, Acta Mater. 185 (2020) 218–232.

[72] M. Hÿtch, E. Snoeck, R.J.U. Kilaas, Quantitative measurement of displacement and strain fields from HREM micrographs, Ultramicroscopy 74 (3) (1998) 131–146.

[73] F. Wu, Y. Zhu, J. Narayan, Macroscopic twinning strain in nanocrystalline Cu, Mater. Res. Lett. 2 (2) (2014) 63–69.

[74] J. Zhang, D. Zhou, X. Pang, B. Zhang, Y. Li, B. Sun, R.Z. Valiev, D. Zhang, Deformation-induced concurrent formation of 9R phase and twins in a nanograined aluminum alloy, Acta Mater 244 (2023) 118540.

[75] S. Xue, Z. Fan, O.B. Lawal, R. Thevamaran, Q. Li, Y. Liu, K. Yu, J. Wang, E. L. Thomas, H. Wang, X. Zhang, High-velocity projectile impact induced 9R phase in ultrafine-grained aluminium, Nat. Commun. 8 (1) (2017) 1653.

[76] C. Niu, C.R. LaRosa, J. Miao, M.J. Mills, M. Ghazisaeidi, Magnetically-driven phase transformation strengthening in high entropy alloys, Nat. Commun. 9 (1) (2018) 1363.

[77] L. Ding, A. Hilhorst, H. Idrissi, P.J. Jacques, Potential TRIP/TWIP coupled effects in equiatomic CrCoNi medium-entropy alloy, Acta Mater 234 (2022) 118049.

[78] D.R. Steinmetz, T. Jäpel, B. Wietbrock, P. Eisenlohr, I. Gutierrez-Urrutia, A. Saeed–Akbari, T. Hickel, F. Roters, D. Raabe, Revealing the strain-hardening behavior of twinning-induced plasticity steels: Theory, simulations, experiments, Acta Mater 61 (2) (2013) 494–510.

[79] G. Laplanche, A. Kostka, O. Horst, G. Eggeler, E. George, Microstructure evolution and critical stress for twinning in the CrMnFeCoNi high-entropy alloy, Acta Mater 118 (2016) 152–163.

[80] H. Wu, G. Fan, An overview of tailoring strain delocalization for strength-ductility synergy, Prog. Mater. Sci. 113 (2020) 100675.

[81] Y. Wang, Y. Wei, Z. Zhao, Z. Lin, F. Guo, Q. Cheng, C. Huang, Y. Zhu, Mechanical response of the constrained nanostructured layer in heterogeneous laminate, Scr. Mater. 207 (2022) 114310.

[82] Y. Wang, C. Huang, Y. Li, F. Guo, Q. He, M. Wang, X. Wu, R.O. Scattergood, Y. Zhu, Dense dispersed shear bands in gradient-structured Ni, Int. J. Plast. 124 (2020) 186–198.

[83] S. Cheng, E. Ma, Y. Wang, L. Kecskes, K. Youssef, C. Koch, U. Trociewitz, K. Han, Tensile properties of in situ consolidated nanocrystalline Cu, Acta Mater 53 (5) (2005) 1521–1533.

[84] N. Jia, F. Roters, P. Eisenlohr, C. Kords, D. Raabe, Non-crystallographic shear banding in crystal plasticity FEM simulations: Example of texture evolution in α-brass, Acta Mater 60 (3) (2012) 1099–1115.

[85] K. Lu, Making strong nanomaterials ductile with gradients, Science 345 (6203) (2014) 1455–1456.

[86] Y. Zhu, X. Wu, Perspective on hetero-deformation induced (HDI) hardening and back stress, Mater. Res. Lett. 7 (10) (2019) 393–398.

[87] D. Wilson, P. Bate, Influences of cell walls and grain boundaries on transient responses of an IF steel to changes in strain path, Acta Mater 42 (4) (1994) 1099–1111.

[88] H. Zhou, C. Huang, X. Sha, L. Xiao, X. Ma, H.W. Höppel, M. Göken, X. Wu, K. Ameyama, X. Han, In-situ observation of dislocation dynamics near heterostructured interfaces, Mater. Res. Lett. 7 (9) (2019) 376–382.

[89] Y. Gu, Z. Li, H. Gao, Hetero-Boundary-Affected Regions in Heterostructured Materials, JOM 75 (5) (2023) 1405–1422.

[90] W. Liu, L. Yu, Y. Liu, H. Sui, H. Fan, H. Duan, Dislocation pile-up polarization model for mechanical properties of polycrystalline metals based on grain boundary resistance variability, J. Mech. Phys. Solids 160 (2022) 104793.

[91] I. Basu, V. Ocelík, J.T. De Hosson, BCC-FCC interfacial effects on plasticity and strengthening mechanisms in high entropy alloys, Acta Mater 157 (2018) 83–95.

[92] T. Chou, W. Li, H. Chang, X. Du, W. Chuang, T. Yang, Y. Zhu, J. Huang, Quantitative analysis of hetero-deformation induced strengthening in heterogeneous grain structure, Int. J. Plast. 159 (2022) 103482.

[93] S. Akarapu, J. Hirth, Dislocation pile-ups in stress gradients revisited, Acta Mater 61 (10) (2013) 3621–3629.

[94] J. Hirth, Dislocation pileups in the presence of stress gradients, Philos. Mag. 86 (25-26) (2006) 3959–3963.

[95] R. Schouwenaars, M. Seefeldt, P. Van Houtte, The stress field of an array of parallel dislocation pile-ups: Implications for grain boundary hardening and excess dislocation distributions, Acta Mater 58 (13) (2010) 4344–4353.

[96] A.H.S. Cottrell, D.L. Dexter, Dislocations and plastic flow in crystals, 1953.

[97] L. Evers, W. Brekelmans, M. Geers, Scale dependent crystal plasticity framework with dislocation density and grain boundary effects, Int. J. Solids Struct. 41 (18-19) (2004) 5209–5230.
[98] S. Zhao, Z. Li, C. Zhu, W. Yang, Z. Zhang, D.E. Armstrong, P.S. Grant, R.O. Ritchie, M.A. Meyers, Amorphization in extreme deformation of the CrMnFeCoNi high-entropy alloy, Sci. Adv. 7 (5) (2021) eabb3108.
[99] C. Slone, S. Chakraborty, J. Miao, E.P. George, M.J. Mills, S.R. Niezgoda, Influence of deformation induced nanoscale twinning and FCC-HCP transformation on hardening and texture development in medium-entropy CrCoNi alloy, Acta Mater 158 (2018) 38–52.
[100] Y. Cai, F. Liu, Y. Tan, L. Wang, X. Ji, S. Xiang, E. A, Synergy effect of multi-strengthening mechanisms in CoNiCr-based high-entropy superalloy at cryogenic temperature, Mater. Sci. Eng. A 901 (2024) 146531.
[101] S. Mahajan, M. Green, D. Brasen, A model for the FCC→ HCP transformation, its applications, and experimental evidence, Metall. Mater. Trans. A 8 (2) (1977) 283–293.
[102] S.L. Wong, M. Madivala, U. Prahl, F. Roters, D. Raabe, A crystal plasticity model for twinning-and transformation-induced plasticity, Acta Mater 118 (2016) 140–151.
[103] X. Zhang, X. Lu, J. Zhao, Q. Kan, Z. Li, G. Kang, Temperature effect on tensile behavior of an interstitial high entropy alloy: Crystal plasticity modeling, Int. J. Plast. 150 (2022) 103201.
[104] G.B. Olson, M. Cohen, A general mechanism of martensitic nucleation: Part I. General concepts and the FCC→ HCP transformation, Metall. Mater. Trans. A 7 (1976) 1897–1904.
[105] V. Nardone, K. Prewo, On the strength of discontinuous silicon carbide reinforced aluminum composites, Scr. Mater. 20 (1) (1986) 43–48.
[106] J. Le, Y. Han, M. Fang, S. Li, G. Huang, J. Mao, C. Boehlert, W. Lu, A universal shear-lag model for accurate assessment of whisker load-transfer strengthening in metal matrix composites, Compos. Part B-eng. 247 (2022) 110317.
[107] H. Ma, Y. Zhao, Z. Lyu, X. Wang, Y. Zhu, Y. Gao, What are the “dispersive shear bands” on the surfaces of layered heterostructured materials? J. Mech. Phys. Solids 181 (2023) 105467.
[108] X. Wang, T. Li, Y. Gao, What really governs the upper bound of uniform ductility in gradient or layered materials? Extrem. Mech. Lett. 48 (2021) 101413.
[109] Y. Wang, Y. Wei, Z. Zhao, H. Long, Z. Lin, F. Guo, Q. He, C. Huang, Y. Zhu, Activating dispersed strain bands in tensioned nanostructure layer for high ductility: the effects of microstructure inhomogeneity, Int. J. Plast. 149 (2022) 103159.
[110] Y. Estrin, Y. Beygelzimer, R. Kulagin, P. Gumbsch, P. Fratzl, Y. Zhu, H. Hahn, Architecturing materials at mesoscale: some current trends, Mater. Res. Lett. 9 (10) (2021) 399–421.
[111] Y.H. Wang, C.X. Huang, Q. He, F. Guo, M. Wang, L.Y. Song, Y. Zhu, Heterostructure induced dispersive shear bands in heterostructured Cu, Scr. Mater. (2019).
[112] W. Abuzaid, H. Sehitoglu, Plastic strain partitioning in dual phase $Al_{13}CoCrFeNi$ high entropy alloy, Mater. Sci. Eng. A 720 (2018) 238–247.